

NEW CONSTRAINTS ON THE NATURE AND ORIGIN OF THE LEADING ARM OF THE MAGELLANIC STREAM

PHILIPP RICHTER¹, ANDREW J. FOX², BART P. WAKKER³, J. CHRISTOPHER HOWK⁴, NICOLAS LEHNER⁴, KATHLEEN A. BARGER⁵, ELENA D'ONGHIA^{3,6}, FELIX J. LOCKMAN⁷

¹Institut für Physik und Astronomie, Universität Potsdam, Haus 28, Karl-Liebknecht-Str. 24/25, 14476 Golm (Potsdam), Germany

²Space Telescope Science Institute, Baltimore, MD 21218, USA

³Department of Astronomy, University of Wisconsin-Madison, 475 N. Charter Street, Madison, WI 53706, USA

⁴Department of Physics, University of Notre Dame, 225 Nieuwland Science Hall, Notre Dame, IN 46556, USA

⁵Department of Physics and Astronomy, Texas Christian University, TCU Box 298840, Fort Worth, TX 76129, USA

⁶Center for Computational Astrophysics, Flatiron Institute, 162 Fifth Avenue, New York, NY 10010, USA and

⁷Green Bank Observatory, P.O. Box 2, Route 28/92, Green Bank, WV 24944, USA

Accepted version from August 25, 2018

ABSTRACT

We present a new precision measurement of gas-phase abundances of S, O, N, Si, Fe, P, Al, Ca as well as molecular hydrogen (H₂) in the Leading Arm (region II, LA II) of the Magellanic Stream (MS) towards the Seyfert galaxy NGC 3783. The results are based on high-quality archival ultraviolet/optical/radio data from various different instruments (HST/STIS, FUSE, AAT, GBT, GB140ft, ATCA). Our study updates previous results from lower-resolution data and provides for the first time a self-consistent component model of the complex multi-phase absorber, delivering important constraints on the nature and origin of LA II. We derive a uniform, moderate α abundance in the two main absorber groups at +245 and +190 km s⁻¹ of $\alpha/H = 0.30 \pm 0.05$ solar, a low nitrogen abundance of $N/H = 0.05 \pm 0.01$ solar, and a high dust content with substantial dust depletion values for Si, Fe, Al, and Ca. These α , N, and dust abundances in LA II are similar to those observed in the Small Magellanic Cloud (SMC). From the analysis of the H₂ absorption, we determine a high thermal pressure of $P/k \approx 1680$ K cm⁻³ in LA II, in line with the idea that LA II is located in the inner Milky Way halo at a z -height of < 20 kpc where it hydrodynamically interacts with the ambient hot coronal gas. Our study supports a scenario, in which LA II stems from the break-up of a metal- and dust-enriched progenitor cloud that was recently (200 – 500 Myr ago) stripped from the SMC.

Subject headings: ISM: abundances – Galaxy: halo – Galaxy: evolution – Magellanic Clouds – quasars: absorption lines

1. INTRODUCTION

The gravitational and hydrodynamical interaction between the Milky Way (MW) and the Magellanic Clouds (MCs) and the subsequent star-formation activity in the Clouds have transported more than one billion solar masses of gas from the MCs into the circumgalactic medium (CGM) of the Milky Way. These processes have produced extended gaseous streams and clouds at distances of $d \approx 20 - 100$ kpc that cover more than 40 percent of the sky (Wannier et al. 1972; Mathewson et al. 1974; Putman et al. 1998; Brüns et al. 2005; Fox et al. 2014; Richter et al. 2017). This gigantic circumgalactic gas reservoir dominates the Milky Way's current and future gas accretion rate (see recent reviews by D'Onghia & Fox 2016; Putman et al. 2012; Richter 2017) and thus has a major impact on the Galaxy's evolution. The neutral gas bodies of these CGM clouds and streams can be observed in H I 21 cm emission, while the more diffuse and more extended ionized gaseous envelopes can be traced in ultraviolet (UV) metal absorption against distant, extragalactic point sources (such as quasars and other type of AGN, for simplicity hereafter referred to as QSOs) as well as in H α emission (see, e.g., Richter 2017; Barger et al. 2013, 2017).

Absorption-line studies of the Milky Way gas environment, in particular, can be readily compared to similar studies of the CGM around other, more distant galaxies

at low and high redshift (e.g., Werk et al. 2013; Stocke et al. 2014; Liang & Chen 2014; Richter et al. 2016). Detailed studies of the spatial distribution and chemical composition of the Milky Way's CGM provide important clues on the on-going formation and evolution of the Galaxy in its Local Group environment through gas infall and satellite interaction. They also deliver detailed constraints on the filling factor and physical conditions of multi-phase circumgalactic gas around star-forming disk galaxies and thus are of high relevance to evaluate the importance of the CGM for galaxy evolution, in general.

The most prominent of the circumgalactic gas features generated by the interaction between the MCs and the MW is the Magellanic Stream (MS), an enormous stream of neutral and ionized gas in the southern hemisphere extending over more than 200 degrees (Nidever et al. 2010), and possibly over several hundred kpc in linear size (D'Onghia & Fox 2016). The main body of the MS is believed to be at a distance of 50 – 100 kpc, thus located in the outer Milky Way halo. The spatial extension of the MS into the northern sky at $l > 300$ is the so-called Leading Arm (LA), a conglomerate of scattered clouds seen in 21 cm data and in UV absorption whose ionized envelope possibly extends far into the northern sky (Fox et al. 2018; Richter et al. 2017). It was previously argued that the LA must be of purely tidal origin, as it leads the orbital motion of the Magellanic System (which includes the MS, the LA, and the Magellanic Bridge) around the

MW (e.g., Putman et al. 1998). However, more recent hydrodynamical simulations indicate that only the combination of multiple tidal stripping events, outflows from the Magellanic Cloud, and ram-pressure stripping can explain the complex spatial distribution of the MS and LA gas components and the observed abundance variations therein (Besla et al. 2010, 2012; Fox et al. 2018; Pardy et al. 2018). The LA, which is sub-divided into four main substructures, LAI-IV (Putman et al. 1998; Brüns et al. 2005; Venzmer et al. 2012; For et al. 2012) is much closer than the MS ($d < 20$ kpc), as evident from the analysis of young stars that recently have been found in the LA (Casetti-Dinescu et al. 2014; Zhang et al. 2017).

In our previous studies, we have used UV absorption-line data for many dozens of QSO sightlines together with 21 cm emission-line data from various instruments to characterize the overall chemical composition of the MS and the LA, to estimate their total mass, and to pinpoint their contribution to the Milky Way’s gas-accretion rate (Fox et al. 2010, 2013, 2014, 2018; Richter et al. 2013, 2017). In addition to these large surveys, detailed analyses for individual sightlines are likewise highly desired. Such studies provide a tremendous amount of accurate information on the chemical enrichment pattern and the local physical conditions in the gas, which is very important to discriminate between different scenarios for the origin of the MS and LA (e.g., LMC vs. SMC). For instance, the substantially higher metallicity and enhanced dust abundance found in the MS along the Fairall 9 sightline (Richter et al. 2013; hereafter referred to as R13) compared to other MS sightlines (Fox et al. 2013) demonstrates that the trailing arm of the MS has a dual origin with spatially and kinematically distinct filaments stemming from both LMC *and* SMC (see also Nidever et al. 2008, 2010). This result sets important constraints for dynamical models of the LMC/SMC/MW gravitational interactions and provides independent evidence for an enhanced star-formation activity in the LMC that has lifted α -enriched gas into the Milky Way halo (see discussions in R13; Bustard et al. 2018; Pardy et al. 2018). The stellar activity of the LMC is currently driving over 10^7 solar masses out of this galaxy in a large-scale galactic wind (Barger 2016) and similar winds were likely generated during episodic periods of elevated star formation in the past.

Following our long-term strategy to explore the origin and fate of the Magellanic System and its role for the past and future evolution of the Milky Way and the Local Group (LG), we here present a detailed study of the chemical abundances and physical conditions in the LAII along the line of sight towards NGC 3783. Because of the brightness of the background Seyfert galaxy NGC 3783 and the high neutral gas column density, the NGC 3783 direction is the best-studied QSO sightline for absorption-line measurements in the LA with a number of detailed studies (Lu et al. 1994, 1998; Sembach et al. 2001; Wakker et al. 2002, hereafter WOP02; Wakker 2006) using medium-resolution UV data from the early-generation HST/UV spectrograph GHRS (Goddard High Resolution Spectrograph), data from the *Far Ultraviolet Spectroscopic Explorer* (FUSE), and 21 cm interferometer data from the Australian Compact Telescope Array

(ATCA). The best available UV data set (in terms of spectral resolution and S/N) for NGC 3783 was obtained using the high-resolution echelle E140M grating of the Space Telescope Imaging Spectrograph (STIS) in 2000–2001 to monitor the UV variability of NGC 3783 and to study its intrinsic absorption (Gabel et al. 2003a, 2003b), but these spectacular STIS spectra never were used to confirm and extend the earlier abundance results in the LA or to use the full diagnostic power of the combined STIS/FUSE/ATCA data set to constrain the physical conditions in the gas. An update of the earlier LA abundance measurements for the NGC 3783 sightline is also highly desired to better characterize the dust-depletion properties of the gas in the LA and to account for the change in the solar reference abundances for the elements sulfur and oxygen since 2002 (Asplund et al. 2009).

With this paper, we are closing this gap and provide the most precise determination of gas and dust abundances in two individual clouds with the LA based on the archival E140M STIS data of NGC 3783. Combining the STIS, FUSE, and ATCA data we further determine important physical quantities such as density, temperature, thermal pressure, and absorber size in the LA. By combining our precision results for the NGC 3783 sightline with our recent measurements of the large-scale metal distribution in the LA based on lower-resolution UV data from the Cosmic Origins Spectrograph (COS; Fox et al. 2018), our multi-instrument spectral survey provides important new constraints on the origin of the LA, its physical properties, and its location in the Milky Way halo.

2. OBSERVATIONS AND DATA ANALYSIS

2.1. *HST/STIS* data

The archival high-resolution STIS data of NGC 3783 ($l = 287.5$, $b = +22.9$) were taken in 2000 and 2001 using the E140M grating as part of the HST proposals 8029 (PI: Kraemer) and 8606 (PI: Crenshaw). The STIS data have a spectral resolution of $R \approx 45,000$, which corresponds to a velocity resolution of $\Delta v \approx 6.6$ km s⁻¹ (FWHM). The signal-to-noise (S/N) in the data is generally very high, reaching up to ~ 45 per resolution element near 1255 Å. This makes this archival spectrum an excellent data set to resolve the LA’s internal velocity-component structure and determine the chemical composition of the gas towards NGC 3783 at high accuracy.

The STIS data were originally reduced with the CALSTIS reduction pipeline (Brown et al. 2002) as part of our earlier study of weak O I absorbers/Lyman-limit systems in the Milky Way halo (Richter et al. 2009), following the strategy outlined in Naranayan et al. (2005). The STIS spectral data of the LA absorption towards NGC 3783 has also been shortly presented in our STIS HVC absorption survey (Herenz et al. 2013), but no detailed analysis of the LA metal abundances based on this superb UV data set has been published so far.

2.2. *FUSE* data

The FUSE data were obtained in 2001 and 2004 (FUSE program IDs E031 and B107; PI: Crenshaw for both proposals) with a total exposure time of 196 ks in the various LiF and SiC spectral channels. The FUSE spectra have a resolution of ~ 20 km s⁻¹ (FWHM), and cover the wave-

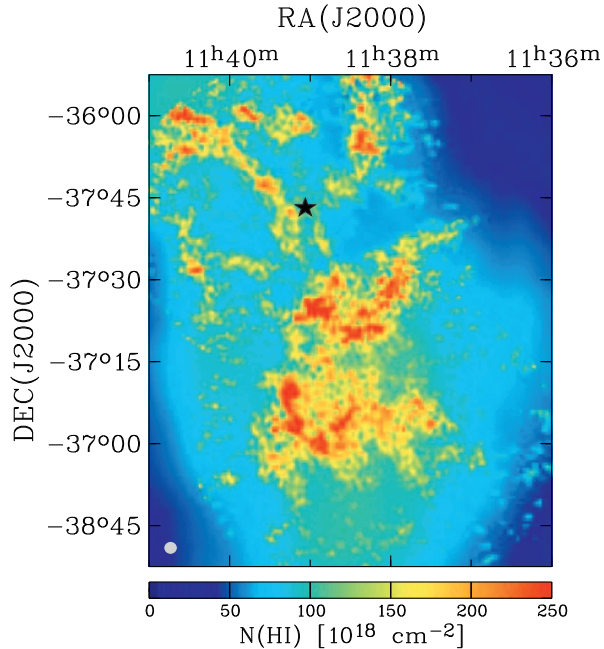


FIG. 1.— H I column-density map of high-velocity gas at $v_{\text{LSR}} = 220 - 260 \text{ km s}^{-1}$ in the LA II region, based on 21 cm emission data from the GB140ft telescope and the ATCA (see Sect. 2.3). The black star symbol marks the position of NGC 3783. The effective beam size is indicated with the gray circle in the lower left corner.

length range $912 - 1180 \text{ \AA}$. The FUSE data were reduced with the CALFUSE reduction pipeline (v.3.2.1). Individual spectra were coadded after correcting for wavelength shifts that are identified by using interstellar lines as wavelength reference. The final S/N per resolution element ranges between 5 and 30, depending on wavelength and spectral channel. It is 24 near 1100 \AA (LiF2 channel), where the most important H_2 lines for the analysis of the LA absorption are located.

Note that an analysis of H_2 absorption in the LA towards NGC 3783 has published earlier by Sembach et al. (2001) and Wakker (2006). While the Sembach et al. (2001) study was based on a small subset of the FUSE data of NGC 3783 available today, the Wakker (2006) study covers the full FUSE data set as analyzed here. Our motivation for re-analyzing the H_2 absorption in the FUSE spectral data is that with the high-resolution STIS data and the detection of neutral carbon (C I) in the LA there is new information on the Doppler parameter (b value) in the H_2 -bearing gas that affects the determination of the H_2 column densities and rotational excitation temperature (see Sect. 4.1).

We complement our UV data set for NGC 3783 from STIS and FUSE with medium resolution (FWHM $\sim 20 \text{ km s}^{-1}$) optical data from the Anglo-Australian Telescope (AAT; as presented in West et al. 1985), which covers the spectral region near the Ca II H&K lines at $3930 - 3980 \text{ \AA}$.

2.3. H I 21 cm data

For our study of the NGC 3783 sightline, we make use of the 21 cm interferometer data from ATCA presented in WOP02, which have a high angular resolution of $1'$. These high-resolution data were combined with single-dish 21 cm data from the Green Bank 140ft telescope

(GB140ft; $21'$ angular resolution) and the Parkes Telescope ($17'$ angular resolution) to construct the final 21 cm spectrum in the NGC 3783 direction (see WOP02; their Sect. 4).

As part of our initial LA metallicity survey (Fox et al. 2018) we also obtained new high-sensitivity 21 cm data for the NGC 3783 sightline from the Robert C. Byrd Green Bank Telescope (GBT; program IDs: GBT12A 206 & GBT17B 424), which provides an angular resolution of $9.1'$ at 1420 MHz. The GBT data cover the LSR velocity range between -450 and $+550 \text{ km s}^{-1}$ at velocity resolution of 0.15 km s^{-1} and were obtained using frequency switching. For the basic data reduction, we followed the procedures outlined in Boothroyd et al. (2011). The rms noise in the GBT spectrum of NGC 3783 is only 11 mK per 0.6 km s^{-1} wide channel, which allows us measure H I column at levels $\leq 3 \times 10^{18} \text{ cm}^{-2}$.

2.4. Spectral analysis

For the determination of the metal abundances in LA II, we use the following (unblended) ion transitions that are available in the combined STIS and FUSE data set: C I $\lambda\lambda 1277.2, 1280.1, 1328.8, 1560.3, 1656.9$, N I $\lambda 1200.7$, N II $\lambda 1084.0$, O I $\lambda 1302.2$, Al II $\lambda 1670.8$, Si II $\lambda\lambda 1190.4, 1193.3, 1260.4, 1304.4, 1526.7$, Si III $\lambda 1206.5$, P II $\lambda 1152.8$, S II $\lambda 1253.8$, and Fe II $\lambda\lambda 1143.2, 1144.9, 1608.5$. Other available transitions in the STIS/FUSE wavelength ranges from these and other ions are either too weak or blended with other absorption lines (e.g., from intervening systems), so that they cannot be used to study absorption in the LA. Atomic data (laboratory wavelengths and oscillator strengths) have been adopted from Morton (2003). For the analysis of the H_2 spectrum, we make use of the H_2 line-compilation from Abgrall & Roueff (1989).

Column densities for the above-listed metal ions have been derived by Voigt-profile fitting and component modeling, as described in detail in R13. In addition, we use the apparent-optical-depth (AOD) method (Savage & Sembach 1991) to measure integrated column densities and to provide a consistency check with the fitting/modeling method. In addition to the column density, the Voigt-profile fitting provides for each LA II absorption component the b value. The b value in the inner, dense core of LA II, as traced by C I, was used as reference value for the modeling of the H_2 absorption in the lower-resolution FUSE data, as C I and H_2 trace the same gas phase (e.g., Spitzer 1978). To validate the results of the H_2 modeling we also construct a curve of growth for blend-free H_2 absorption lines, as described in the Appendix.

Note that in this study, we do not re-analyze the absorption of higher ions (e.g., O VI, C IV, Si IV) in the combined STIS/FUSE data set, but concentrate instead on the metal abundances and physical conditions in the weakly-ionized, cooler gas in the core of LA II.

3. STRUCTURE AND CHEMICAL COMPOSITION OF LA II

3.1. Component structure

In Fig. 1 we show the sky position of the NGC 3783 sightline (black solid star symbol) overlaid on the 21 cm emission map of the LA gas distribution from the combined ATCA/Parkes data (WOP02) in the velocity range

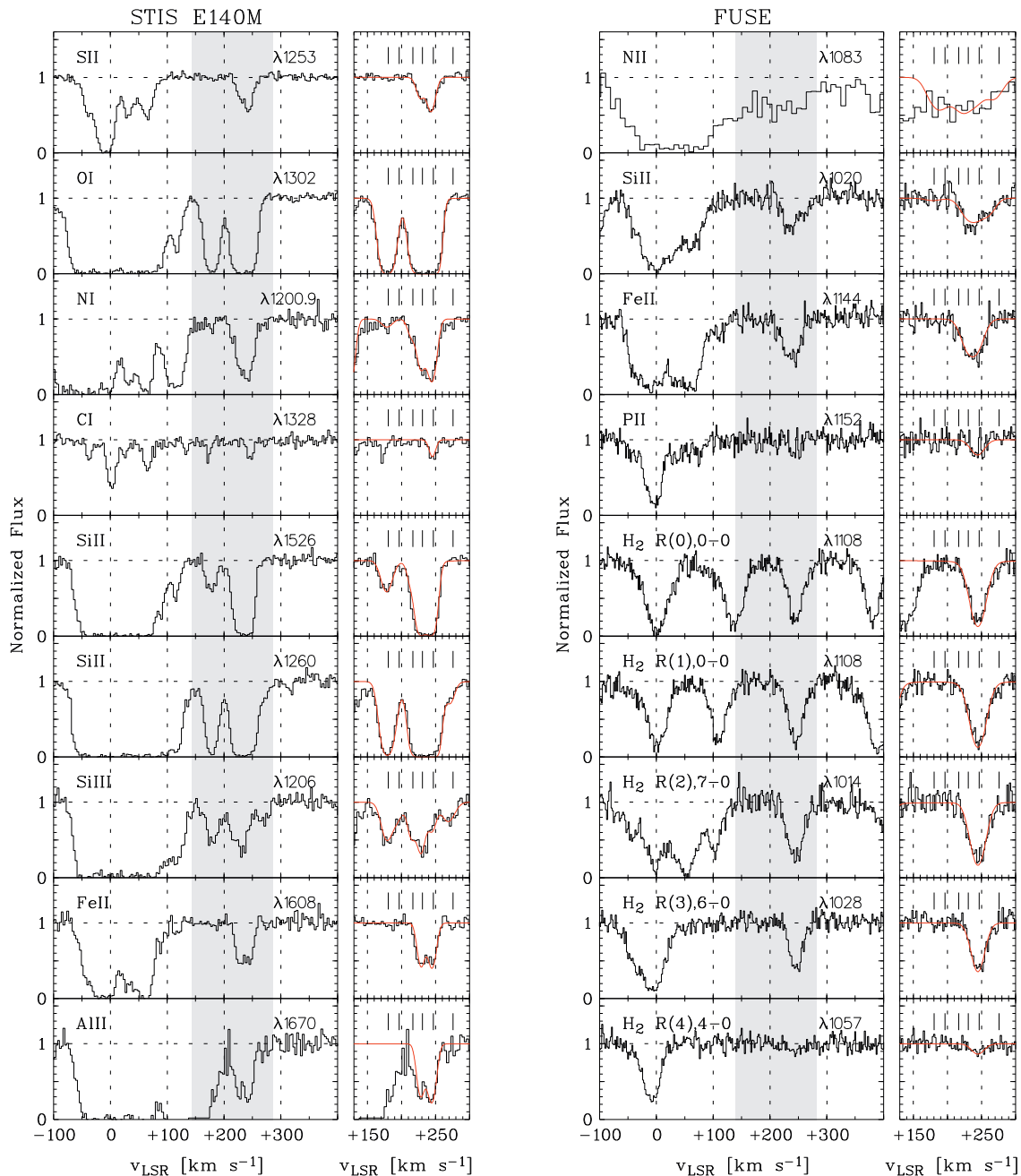


FIG. 2.— Velocity profiles of various metal ions and H₂ (Left column: STIS E140M data; Right column: FUSE data). The gray-shaded area indicates the LA velocity range. The red solid line shows the best-fitting result from the component modeling with the black tick-marks displaying the six identified LA velocity components. We do not show other available metal transitions that are either blended with other absorption features or too weak to show significant absorption in LA II.

$v_{\text{LSR}} = 220 - 260 \text{ km s}^{-1}$. As discussed in WOP02, the NGC 3783 sightline does not pass through any of the peaks in the 21 cm column-density distribution, but passes it at a column-density valley. The observed angular fine-structure in the 21 cm emission map at arcmin scale underlines that a precise estimate of the H I column density in the LA along the NGC 3783 sightline cannot be obtained from lower-resolution single-dish 21 cm data alone.

In Fig. 2 we show the velocity profiles of various metal ions and H₂ from the STIS E140M and FUSE data of NGC 3783. The velocity range that is expected for ab-

sorption from the LA ($v_{\text{LSR}} = +140$ to $+300 \text{ km s}^{-1}$; Putman et al. 1998) is shown as gray-shaded area. In this range, we identify six individual velocity components at $v_{\text{LSR}} = +179, +195, +215, +229, +245, +269 \text{ km s}^{-1}$. The dominating neutral gas component (in terms of the neutral gas column density) is located at $+245 \text{ km s}^{-1}$ (comp. 1), coinciding in velocity with the dominating 21 cm emission peak seen in the 21 cm data (Fig. 3). This component is detected in absorption in O I, N I and in all singly-ionized species, as well in C I and H₂. The simultaneous detection of neutral carbon and molecular hydrogen at moderate strength already indicates that this

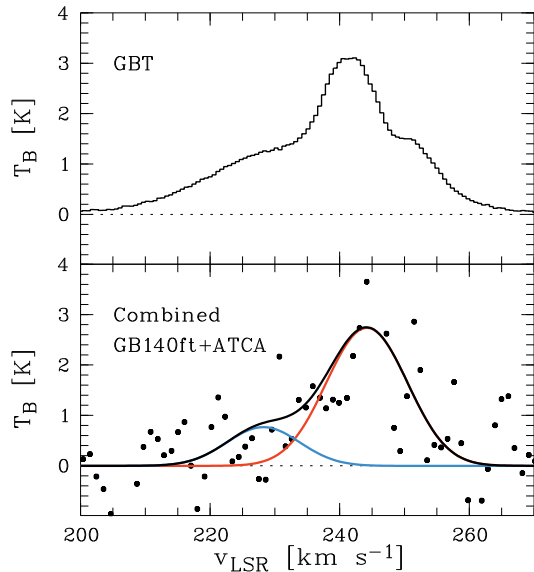


FIG. 3.— *Upper panel:* H I 21 cm emission spectrum in the NGC 3783 direction from the GBT (at 9.1' resolution) in the velocity range $v_{\text{LSR}} = 200 - 270 \text{ km s}^{-1}$. *Lower panel:* combined ATCA/GB140 ft data set (at 1' resolution; black dots) from WOP02 for the same sightline/velocity range, overlaid with a two-component fit (black solid line) and two fitted components as individual profiles (red and blue solid lines).

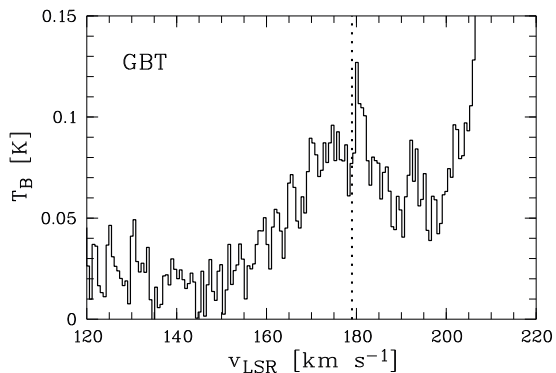


FIG. 4.— Zoom-in of the GBT 21 cm spectrum towards NGC 3783 in the velocity range $v_{\text{LSR}} = 120 - 220 \text{ km s}^{-1}$. Very weak but significant emission is seen in a broad component centered at $v_{\text{LSR}} \approx 175 - 180 \text{ km s}^{-1}$, associated with the O I/Si II absorption component at $+179 \text{ km s}^{-1}$ (dashed line; see also Fig. 2).

component harbors predominantly neutral gas that is relatively cold and dense (a phase that is referred to as “cold neutral medium”, CNM). The $+245 \text{ km s}^{-1}$ component is accompanied by a weaker satellite component at $+229 \text{ km s}^{-1}$ (comp. 2), which gives the unsaturated or only mildly saturated LA absorption features of Si II, Ni I, Si III, P II, Fe II, and Al II at $+220 - 260 \text{ km s}^{-1}$ an asymmetric shape (Fig. 2).

Another major absorption component is seen at $+179 \text{ km s}^{-1}$ (comp. 3) in the strong lines of O I and Si II (also seen in Si III and, very weak, in Ni I), accompanied by its own satellite component at $+195 \text{ km s}^{-1}$ (comp. 4). Two additional, very weak satellite components at $+215 \text{ km s}^{-1}$ (comp. 5) and $+269 \text{ km s}^{-1}$ (comp. 6) are visible only the strong lines of Si II and Si III.

3.2. H I 21 cm emission

3.2.1. Velocity range 200 – 280 km s^{-1}

In view of the complex velocity-component structure of LA II seen in the STIS data we decided to re-fit also the combined ATCA 21 cm data originally presented in WOP02. In Fig. 3 we compare the new 9.1'-resolution GBT spectrum for the NGC 3783 direction (upper panel) with the 1'-resolution data from ATCA (lower panel, black dots; from WOP02). The GBT data show a beam-smearred version of the H I distribution in the general direction of NGC 3783, with the main emission peak located at $v_{\text{LSR}} = +241 \text{ km s}^{-1}$, an extended wing at lower velocities down to $\sim +210 \text{ km s}^{-1}$, and a weak bump at $\sim 250 \text{ km s}^{-1}$. This velocity-component structure slightly deviates from the one seen in absorption (see above). This demonstrates that in this particular direction (Fig. 1) small-scale structure exists in the 21 cm distribution that is not fully resolved in the 9.1' beam of the GBT. This aspect emphasizes the need for using interferometer data to determine an accurate H I column-density estimate in LA II towards NGC 3783.

In WOP02, the combined 1'-resolution ATCA data for the NGC 3783 direction was fitted with a single-component Gaussian centered at $v_{\text{LSR}} = +244 \text{ km s}^{-1}$, yielding an H I column density of $N(\text{H I}) = (8.26 \pm 1.98) \times 10^{19} \text{ cm}^{-2}$ (see their Fig. 9). However, the STIS data of NGC 3783 demonstrates that there are *two* main neutral components close together at $+245 \text{ km s}^{-1}$ (comp. 1) and $+229 \text{ km s}^{-1}$ (comp. 2; see Table 1). Also the GBT data indicate that neutral gas near $+229 \text{ km s}^{-1}$ must be indeed present on larger angular scales in the general NGC 3783 direction. We therefore re-fitted the combined ATCA data with a two-component fit, where the center velocities were fixed to the absorption velocities of comp. 1 and 2 at $+245$ and $+229 \text{ km s}^{-1}$. Also the FWHM of the two fitted emission components were fixed. They were calculated from the b values of comp. 1 and 2. We thus are explicitly assuming that the b values reflect only the internal velocity dispersion in the gas and thermal broadening is negligible. This is justified in view of the expected very small contribution of thermal line-broadening to b for metal lines in cold neutral gas.

The fit to the raw ATCA data is shown in the lower panel of Fig. 3 with the black solid line, while the red and blue solid lines indicate the individual shapes of comp. 1 and 2, respectively. This two-component fit yields column densities of $N(\text{H I}) = 7.71 \times 10^{19} \text{ cm}^{-2}$ for comp. 1 and $N(\text{H I}) = 1.94 \times 10^{19} \text{ cm}^{-2}$ for comp. 2. The total H I column density then comes out to $N(\text{H I}) = (9.65 \pm 1.67) \times 10^{19} \text{ cm}^{-2}$ or $\log N(\text{H I}) = 19.98^{+0.07}_{-0.08}$. This is ~ 16 percent higher than the value given in WOP02, but both values formally agree at the 1σ level. To verify the robustness of the fit and to account for the large scatter in the noisy T_B distribution we also binned the ATCA data applying different bin sizes (ranging from 3 to 6 pixels) and different binning-starting points. However, we do not find any significant deviations from the fit to the raw data.

We note that for $T \approx 100 \text{ K}$ and $b \approx 7 \text{ km s}^{-1}$ the opacity in the 21 cm line is ≤ 4 percent in comp. 1 and 2 (see Dickey & Lockman 1990) and much smaller in all other components. Therefore, any possible corrections related to the 21 cm line opacity are negligible compared to the 17 percent uncertainty that we quote on $N(\text{H I})$

from the fit of the ATCA data.

In the following abundance determination, we therefore use the value $\log N(\text{HI}) = 19.98_{-0.08}^{+0.07}$ for the total neutral gas column density in comp. 1+2.

3.2.2. Velocity range 150 – 200 km s⁻¹

Because of the very high quality of the GBT data (noise level is 11 mK per 0.6 km s⁻¹ wide channel) the GBT spectrum allows us to search for weak emission from neutral gas that is associated with the +179 km s⁻¹ absorption component (comp. 3) seen in O I, N I, Si II, and Si III (see Table 1).

In Fig. 4 we show a zoom-in into the GBT spectrum in the velocity range between +120 and +220 km s⁻¹ for $T_B \leq 150$ mK. A broad, weak emission peak is clearly visible near +180 km s⁻¹. Integration of T_B over the velocity range +155 to +215 km s⁻¹ yields a column density of $N(\text{HI}) = (4.70 \pm 1.35) \times 10^{18}$ cm⁻² or $\log N(\text{HI}) = 18.67_{-0.15}^{+0.11}$. The neutral gas-column density of the component at +179 km s⁻¹ thus is ~ 20 times smaller than $N(\text{HI})$ in the main LA II components near +240 km s⁻¹.

3.3. Absorption-profile fitting and modeling

For the quantitative analysis of the observed absorption pattern, we reconstructed the component structure by combining Voigt-profile fitting and component modeling (see also R13). For this, we simultaneously fitted the (relatively weak absorption) lines of Si II $\lambda 1253.8$, N I $\lambda 1200.7$, Si III $\lambda 1206.5$, Al II $\lambda 1670.8$, and Fe II $\lambda 1608.5$ in the STIS data to determine the center velocities, b -values, and column densities, N , for these ions in comp. 1 and 2. We then fixed the velocities and b -values for these two components and fitted (as the only free parameter) the column densities for the remaining two ions that show only strongly saturated absorption in these components (O I and Si II). For the remaining four absorption components, we then obtained center velocities, b -values, and column densities by simultaneously fitting those (strong) lines in which these (weak) components show up. In this way, we have constructed a final component model for which we have generated a synthetic spectrum taking into account the spectral resolution of the STIS and FUSE instruments. This synthetic spectrum is shown in Fig. 2 with the red solid line. 1σ column-density errors have been derived by varying N in the model in the allowed range, as constrained by the residuals between the model spectrum and the data (see also R13, their App. B). All results from the fitting/modeling procedure are summarized in Table 1.

As it turns out, all metal ions except C I can be fitted by assigning a fixed center velocity and a fixed b -value to each component. The five C I lines at $\lambda 1277.2$, 1280.1, 1328.8, 1560.3, 1656.9 Å, that show absorption in the LA in comp. 1 at +245 km s⁻¹ are too narrow to be reproduced by the b -value of 7.3 km s⁻¹ that is derived from the fitting/modeling of the singly-ionized species and O I/N I. If we fit the C I lines individually, we obtain a b -value of (5.0 ± 0.6) km s⁻¹. The smaller b -value for C I indicates that the neutral carbon resides in sub-structure within comp. 1 that is spatially more confined than the region that hosts O I/N I and the

singly ionized species, reflected by a smaller velocity dispersion in the gas. This trend is not surprising, however. The ionization potential of neutral carbon is only 11.26 eV and therefore substantial amounts of C I can exist only in relatively dense regions where the recombination rate is sufficiently high to compensate for the photoionization. We conclude that the C I absorption arises in a small, dense gas clump within comp. 1 that is surrounded by more diffuse gas (the latter phase in comp. 1 also being traced by the other ions that have higher ionization potentials).

The fact that we derive a b -value for C I in comp. 1 that is lower than for the other ions has implications for the absorption-line modeling of the LA molecular hydrogen absorption in the FUSE data. From previous UV absorption-line studies it is well known that neutral carbon co-exists with H₂ in the same gas phase (e.g., Spitzer 1978), so that $b(\text{H}_2) = b(\text{C I}) = (5.0 \pm 0.6)$ km s⁻¹ is expected. This value is very similar to the value derived in Wakker (2006). In the Appendix, we provide another, independent measurement of $b(\text{H}_2)$ from the curve-of-growth analysis of selected H₂ lines from different rotational levels.

For Ca II $\lambda 3934$, we adopt the equivalent-width measurement in LA II from the AAT data, as presented in West et al. (1985). These authors measure $W_{3934} = (50 \pm 15)$ mÅ in comp. 1+2, which translates to a column density of $\log N(\text{Ca II}) = 11.76_{-0.15}^{+0.11}$.

3.4. Metal abundances

Based on the modeled ion column densities listed in Table 1 we obtain the relative gas-phase abundance for an element M compared to the solar abundance in the standard way

$$[\text{M}/\text{H}] = \log(\text{M}_X/\text{HI}) + \text{IC}(\text{M}_X) - \log(\text{M}/\text{H})_{\odot}, \quad (1)$$

where X is an ion of the element M, $\text{IC}(\text{M}_X)$ is the ionization correction for that ion, and $\text{M}/\text{H}_{\odot}$ is the solar reference abundance for M. The results and assumed parameters are summarized in Table 2.

As solar reference abundances we use the values listed in Asplund et al. (2009), which deviate (substantially for some elements) from those used in the earlier LA abundance measurements for the NGC 3783 sightline. For example: Lu et al. (1998) used a value of $(\text{S}/\text{H})_{\odot} = -4.73$ dex from Anders & Grevesse (1989) for their metallicity determination of LA II, while Asplund et al. (2009) gives $(\text{S}/\text{H})_{\odot} = -4.88$ dex, thus 0.15 dex lower (see also Howk et al. 2005).

3.4.1. Ionization corrections

Although most of the metal ions listed in Table 1 represent the dominant ionization states in neutral interstellar gas (C I and Ca II being the exception), their ionization potentials are different from that of H I so that ionization corrections (ICs) generally need to be considered. The neutral-gas column density in comp. 1+2 is almost 10^{20} cm⁻² so that here the ICs are expected to be small. For comp. 3, which has $\log N(\text{HI}) = 18.67$, the ICs are expected to be more severe and strongly dependent on the local gas density.

TABLE 1
SUMMARY OF COLUMN-DENSITY MEASUREMENTS

Component ^a		1	2	3	4	5	6			
v [km s ⁻¹]		+245	+229	+179	+195	+215	+269			
b [km s ⁻¹]		7.3 (5.0 ^b)	6.6	10.0	9.0	6.5	12.0			
Ion/Species	Instrument	log N_1	log N_2	log N_3	log N_4	log N_5	log N_6	log $N_{1+2, \text{model}}$	log $N_{1+2, \text{AOD}}^c$	log $N_{3, \text{AOD}}^c$
H I	ATCA+GB140ft	19.98 ^{+0.07} _{-0.08}	...
	GBT	18.69 ^{+0.11} _{-0.15}
C I	STIS	13.00	12.80	13.05 ± 0.04	13.03 ± 0.04	...
C I*	STIS	≤ 12.75	...
C I**	STIS	≤ 12.40	...
C II*	STIS	≤ 12.93	...
N I	STIS	14.30	14.05	13.20	...	13.43	...	14.49 ± 0.06	14.46 ± 0.06	13.14 ± 0.10
N II	FUSE	13.39	13.51	13.50	13.50	13.46	13.50	13.72 ± 0.09	13.84 ± 0.11	...
O I	STIS	15.90	15.60	14.90	13.30	14.20	...	16.08 ± 0.64	≥ 15.14	≥ 14.69
Al II	STIS	12.45	12.31	12.69 ± 0.06	12.72 ± 0.06	...
Si II	STIS+FUSE	14.19	14.14	13.28	11.84	12.98	11.48	14.61 ± 0.05	14.55 ± 0.08	13.24 ± 0.08
Si III	STIS	12.14	12.48	12.41	11.90	12.23	12.11	12.62 ± 0.07	12.57 ± 0.09	12.49 ± 0.06
P II	FUSE	12.90	12.90 ± 0.06	12.73 ± 0.13	...
S II	STIS	14.40	14.08	14.57 ± 0.03	14.59 ± 0.03	≤ 13.40
Fe II	STIS+FUSE	13.72	13.66	13.99 ± 0.06	13.99 ± 0.05	≤ 12.80
Ca II	AAT	11.76 ^{+0.11} _{-0.15}	...
H ₂ , $J = 0$	FUSE	18.00	18.0 ± 0.4
H ₂ , $J = 1$	FUSE	17.80	17.8 ± 0.4
H ₂ , $J = 2$	FUSE	16.40	16.4 ± 0.2
H ₂ , $J = 3$	FUSE	15.20	15.2 ± 0.2
H ₂ , $J = 4$	FUSE	14.00	14.0 ± 0.2
H ₂ , total	FUSE	18.22	18.2 ± 0.4

^a Velocity centroids and b -values are kepted fix in the component model; see Sect. 3.3.

^b Only for C I and H₂.

^c Transitions used to dermine column desities via the AOD method: H I 21cm, C I $\lambda\lambda$ 1328, 1377, N I $\lambda\lambda$ 1134, 1200, N II λ 1083, O I λ 1302, Al II λ 1670, Si II $\lambda\lambda$ 1193, 1020, Si III λ 1206, P II λ 1152, S II λ 1253, Fe II $\lambda\lambda$ 1144, 1608. The adopted velocity range is 200 – 280 km s⁻¹.

To quantitatively estimate the ICs, we follow the strategy outlined in our earlier MS/LA studies (Fox et al. 2013, 2014, 2018; R13). From the photoionization modeling with the *Cloudy* code (Ferland et al. 2013), we calculate the IC for each ion. This calculation is based on the local neutral gas column density in comp. 1+2 and comp. 3 and an estimate of the local ionization parameter, U , which is the ratio between ionizing photon density and the gas density in the cloud. The local photon density (in units cm⁻³) in LA II is set to $\log n_\gamma = -5.55$. This value is adopted from the 3-D Galactic radiation field model of Fox et al. (2014), which takes into account the direction of the NGC 3783 sightline and an assumed distance of LA II of 20 kpc.

The local value for U can estimated from the measured Si III/Si II column density ratios, an approach that has been used in many of our previous studies of the MS and the LA (see Fox et al. 2013, 2014, 2018; R13). One drawback of this method is that it does not account for the possible multi-phase nature of the absorbers that may be composed of denser cores and more diffuse gas layers where the local Si III/Si II ratios may vary considerably. In predominantly ionized gas layers, for example, Si III will dominate over Si II, but most of the total Si II column density comes from the densest regions. This is aspect is relevant particularly for low-column density CGM absorbers, where Si II/Si III/Si IV often are believed to trace different gas phases. Evidence for this comes from the fact that for many absorbers a single-component *Cloudy* model cannot reproduce the observed column-density ratios of these ions (Muzahid et al. 2018; Richter

et al. 2016), indicating that they are likely not be well mixed. Therefore, the absolute values for the ICs derived from the observed Si III/Si II column-density ratios, which represent sightline-averages per definition, should be regarded as upper limits. They add to the total error budget for determining $[M/H]$ as a result of the unknown density structure within the absorbers.

3.4.2. Components 1 & 2

From the observed Si III/Si II column density ratio in comp. 1+2 (Table 1, column 9), we infer a value of the ionization parameter of $\log U = -3.4$. The resulting ICs for each ion in comp. 1+2 are listed in the sixth column of Table 2. At this high neutral gas column density, the ICs are all very small, as expected (their absolute values are ≤ 0.03 dex for N I, O I, Al II, P II, and S II) and 0.09 and 0.12 dex for Fe II and Si II, respectively). These numbers demonstrate that ionization effects have only a very minor influence on the determination of metal abundances in comp. 1+2. The resulting values for $[M/H]$, derived by using equation (1), are listed in the seventh column of Table 2.

The well-resolved, unsaturated S II λ 1253.8 absorption in this STIS spectrum has a very high S/N of 35 per resolution element. This line provides the most precise constraint of the α abundance in LA II. Unfortunately, the two other available S II lines at 1250.6 and 1259.5 Å are blended with other absorption features. At the given H I column density in comp. 1+2, the IC for S II is zero (see Table 2), minimizing the systematic error for determining $[S/H]$. In addition, sulfur is not depleted into dust grains

(such as the α element Si; Savage & Sembach 1996). Our measurement of $\log N(\text{Si II}) = 14.57 \pm 0.03$ in comp. 1+2 translates into a sulfur abundance of $[\text{S}/\text{H}] = -0.53 \pm 0.08$ (0.30 ± 0.05 solar). This value is 0.07 dex higher than the previous estimate from Lu et al. (1998), but most of this discrepancy is due to the use of different solar reference abundances (see above) and different values for $N(\text{H I})$, while the values for $N(\text{Si II})$ are identical. The value of $[\text{S}/\text{H}] = -0.53 \pm 0.08$ in comp. 1+2 from the STIS data is higher than the value derived by us from the lower-resolution COS data (Fox et al. 2018; $[\text{S}/\text{H}] = -0.63 \pm 0.16$), but is consistent within the 1σ error range. A more detailed comparison between the STIS and the COS data is presented in the Appendix.

Also for O I and P II ionization corrections and dust depletion effects are unimportant for the determination of $[\alpha/\text{H}]$, but the O I $\lambda 1302.2$ line is strongly saturated (Fig. 1), so that $\log N(\text{O I})$ is uncertain (Table 1). The P II $\lambda 1152.8$ line lies in the FUSE wavelength range and is unsaturated, but has a S/N of only 12 per resolution element, thus substantially lower than the S II $\lambda 1253.8$ line. Still, the derived abundances of $[\text{O}/\text{H}] = -0.60 \pm 0.27$ and $[\text{P}/\text{H}] = -0.48 \pm 0.09$ agree very well within their error range with the above given S abundance. Therefore, the observed abundance of phosphorus provides additional strong constraints on the α abundance in LA II towards NGC 3783. We discuss elements that are known to be depleted into dust grains (e.g., Si, Fe, Al, and Ca; Savage & Sembach 1996) in Sect. 3.6.

For nitrogen, we derive $[\text{N}/\text{H}] = -1.31 \pm 0.09$ in comp. 1+2, thus substantially lower than for α elements. Note that the lower abundance of N cannot be explained by an ionization effect. The *Cloudy* model indicates that the IC for N I in comp. 1+2 is only -0.03 dex, in line with the observed low column density of N II, which is 0.75 dex below that of N I. This is the first measurement of the nitrogen abundance in the LA. A similarly low value has been found in the main body of MS (Fox et al. 2013) and in the MS-LMC filament (R13). The resulting $[\text{N}/\alpha]$ ratio in LA II is -0.77 dex, a value that is also typical for other low-metallicity MW halo clouds (e.g., Richter et al. 2001) and DLAs at low and high redshift (e.g., Pettini 2008; Petitjean et al. 2008). A low $[\text{N}/\alpha]$ ratio is typical for environments that are enriched predominantly by SNe Type II (see discussion in R13).

3.4.3. Component 3

From our *Cloudy* modeling of comp. 3, we find that the ionization correction for O I is negligible for gas densities of $\log n_{\text{H}} \geq -3$, which is not surprising as both hydrogen and oxygen have the nearly identical first ionization potentials. Therefore, the O I/H I ratio provides a reliable measure for the oxygen abundance also in comp. 3. From our measurements listed in Table 1 we derive $[\text{O}/\text{H}] = -0.46 \pm 0.24$, which is (within the error range) identical to the value derived for comp. 1+2. The large error in this abundance estimate is due to the saturation of the O I $\lambda 1302$ line (Fig. 2).

For the determination of gas-phase abundances (or upper limits) for the other elements (N, Si, C, Fe, S) we have set up another *Cloudy* model assuming $\log N(\text{H I}) = 18.67$ and an overall metallicity of 0.3 solar. The *Cloudy* model plot, which shows the predictions for ion column densities as a function of ionization parameter

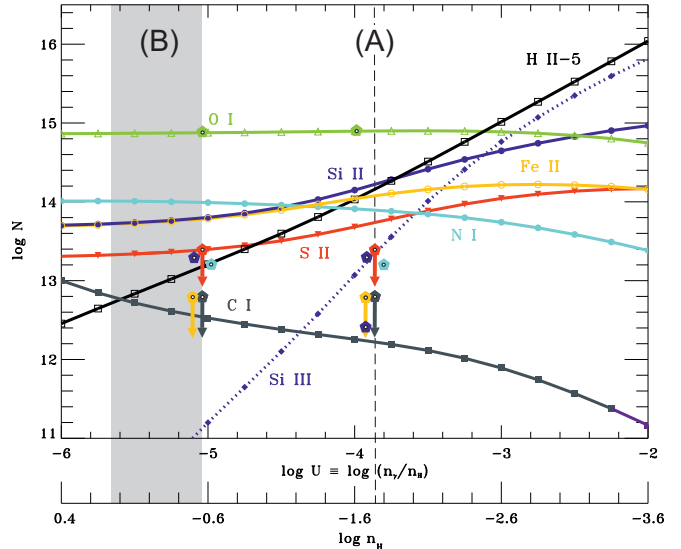


FIG. 5.— Predicted ion column densities vs. ionization parameter (U) and gas density (n_{H}) from the *Cloudy* model of comp. 3. The model-input parameters are: $\log N(\text{H I}) = 18.67$, $[\text{M}/\text{H}] = -0.53$, $\log n_{\gamma} = -5.5$. The two possible model solutions, (A) and (B), are discussed in Sect. 3.4.3.

U , is shown in Fig. 5. If we take the observed Si III/Si II in comp. 3 as the basis (Table 1), the *Cloudy* model delivers $\log U = -3.86$ ($\log n_{\text{H}} = -1.74$) as unique solution (hereafter referred to as Model (A); dashed line in Fig. 5). At this value of U , however, the observed column densities (or upper limits) for S II and Si II do not match the expectations from the *Cloudy* model for a uniform α abundance of 0.3 solar. Instead, the sulfur abundance would need to be lowered to a value of 0.14 solar and the Si abundance to a value of 0.03 to make the *Cloudy* model with $\log U = -3.86$ fit the data. Depletion into dust grains could explain some of the predicted underabundance of Si (see next section), but not all of it, while S is not expected to be depleted into dust at a significant level. Abundance anomalies for S and other α elements have been found in intervening metal absorbers (e.g., Fox, Anne et al. 2014; Richter et al. 2005a), but not in Galactic halo clouds. In view of the solar S/O ratio in comp. 1+2 it would be difficult to explain why S and Si are substantially underabundant compared to O just in this particular region of the LA.

If, however, only a fraction of the observed Si III column density in comp. 3 is co-spatial with Si II (i.e., if the absorber is multi-phase), then the value of $\log U = -3.86$ represents only an upper limit (see discussion in Sect. 3.4.1) and other solutions for $\log U$ and $\log n_{\text{H}}$ are allowed. If we ignore Si III and instead fix the S/O ratio in comp. 3 to the solar value and further take into account that C I is not detected in comp. 3, the *Cloudy* model gives the ranges $\log U = -5.65$ to -5.05 and $\log n_{\text{H}} = -0.55$ to $+0.05$ as allowed solutions (Model (B); gray-shaded area in Fig. 5). In this range for U , the metal abundances come out as $[\text{O}/\text{H}] = -0.53 \pm 0.24$, $[\text{S}/\text{H}] \leq -0.52$, $[\text{N}/\text{H}] = -1.30 \pm 0.14$, $[\text{Si}/\text{H}] = -1.02 \pm 0.15$, and $[\text{Fe}/\text{H}] \leq -1.50$, thus (within the uncertainties) identical to the abundances derived for comp. 1+2. In view of the fact that Si III is known to be non-cospatial in many CGM absorbers (Richter et al. 2016) and Model (B) does not require any significant abundance anomalies within

the family of α elements (O, S, Si), we regard Model (B) as the far more realistic solution to the *Cloudy* output. In the following, we therefore concentrate on Model (B) and do not any further consider Model (A). Model (B) implies that the $+179 \text{ km s}^{-1}$ component represents a relatively dense ($n_{\text{H}} \geq 0.3 \text{ cm}^{-3}$) clump that is well separated from the main body of LA II in velocity (possibly also in space), but that has the same origin.

3.4.4. Comparison with LMC/SMC abundances

In Fig. 6 we compare the LA II abundances in comp. 1+2 and comp. 3 from this study with photospheric abundances in the SMC and LMC taken from the abundance compilations presented in Tchernyshyov et al. (2015) and Jenkins & Wallerstein (2017; see references therein). The similarity between the LA II abundances in comp. 1–3 and the SMC abundance pattern for non-depleted species (O, S, P, N) is striking. Within the error bars, the abundances for these elements are identical in LA II and in the stellar body of the SMC, while the LMC abundances are all systematically higher.

For the interpretation of Fig. 6, it is important to note that the chemical composition of the LA II today should reflect the ISM abundance in the host galaxy at the time when LA II was separated from its host, unless the recently detected stellar population in the LA (Casetti-Dinescu et al. 2014; Zhang et al. 2017) has injected substantial amount of metals to increase the abundance in the gas. Even then, the SMC-like abundance pattern in LA II today is in line with the idea that LA II has been recently separated from the SMC (a few hundred Myr ago; see Pagel & Tautvaivsiene 1998; Harris & Zaritsky 2004). This scenario is also supported by the predominantly low α -abundances observed in other regions of the LA (Fox et al. 2018). We will further discuss these aspects in Sect. 4.

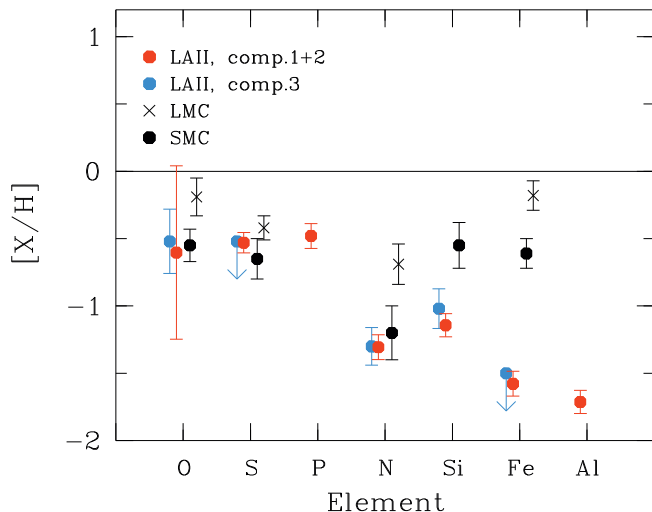


FIG. 6.— Gas-phase metal-abundances in LA II towards NGC 3783, as derived from our STIS/FUSE data set. The first three elements (O, S, P) represent α elements that are not expected to be depleted into dust grains. The following four elements are known to be underabundant in interstellar environments either because of nucleosynthetic effects (N, Fe) and/or due to dust depletion (Si, Fe, Al). Photospheric abundances in the LMC and SMC are shown for comparison (adopted from Tchernyshyov et al. 2015 and Jenkins & Wallerstein 2017 and references therein).

3.5. Molecular hydrogen abundance

The molecular hydrogen absorption in the LA II is confined to comp. 1, where also the C I is observed. The total H_2 column density, as derived from summing over all rotational levels J (see Table 1), is $\log N(\text{H}_2) = 18.2 \pm 0.4$. From the modeling of ATCA 21 cm data follows that 80 percent of the observed neutral hydrogen column in LA II of $\log N = 19.98$ resides in comp. 1, so that $\log N_1 = 19.88$. The neutral gas column in the $\text{H}_2/\text{C I}$ bearing gas clump most likely is even smaller. This is evident from the lower b -value of the $\text{H}_2/\text{C I}$ absorption, which indicates the presence of a dense, spatially confined substructure in comp. 1 that carries only an (unknown) fraction of the total H I column in this component. The lower limit for the (local) fraction of hydrogen in molecular form in this sub-clump then is $\log f_{\text{H}_2} \equiv \log [2N(\text{H}_2)/(N(\text{H I}) + 2N(\text{H}_2))] \geq -1.38$. This logarithmic fraction is 0.65 dex higher than the H_2 fraction observed in the LMC filament of the MS towards Fairall 9 (R13). The interpretation of this difference requires a thorough modeling of the H_2 formation-dissociation equilibrium, which will be discussed in Sect. 4.1 and in the Appendix.

3.6. Dust depletion

The significant underabundance of the elements Si, Fe, Al, and Ca in comp. 1+2 and comp. 3 (see Table 2 and Sect. 3.4.3) indicates the presence of interstellar dust grains (e.g., Savage & Sembach 1996). Also the presence of H_2 in comp. 1 hints at significant amounts of dust in LA II, because hydrogen molecules can form efficiently only on the surfaces of dust grains (e.g., Spitzer 1978). For Fe, in addition, part of the underabundance might be explained by nucleosynthetic effects, namely the delayed production of Fe-peak elements from core collapse and Type Ia supernovae (Tsujiimoto et al. 1995). Following the formalism described in R13, we define for each element M the logarithmic depletion value as $\log \delta(M) = [M/H]_{\text{LA}} - [M/H]_{\text{LA}}$. Using this definition, we derive the following the depletions values: $\log \delta(\text{Si}) = -0.5$ to -0.6 dex, $\log \delta(\text{Fe}) \geq -1.1$, $\log \delta(\text{Al}) = -1.2$, and $\log \delta(\text{Ca}) \geq -1.4$. Due to the possible underabundance of Fe-peak elements in the gas, only a lower limit for $\delta(\text{Fe})$ can be given. If we take the Fe abundance in the SMC as reference, the Fe depletion in LA II is $\log \delta(\text{Fe}) = -1.0$. For Ca, the upper limit for $\delta(\text{Ca})$ is a result of the unknown ionization correction for Ca II, which strongly depends on the (unknown) gas density structure within comp. 1+2 and thus cannot be constrained by our *Cloudy* model.

The (absolute) depletion values for Si and Al (and possibly also Fe and Ca) are significantly larger than what we had found in the LMC filament of the MS towards Fairall 9, suggesting that the dust-to-gas ratio in LA II is (at least locally) higher. This is quite surprising, because the metallicity in LA II is *lower* than in the LMC filament of the MS (R13). These interesting findings will be further evaluated in Sect. 5.2.

4. PHYSICAL CONDITIONS IN LA II

4.1. H_2 diagnostics

Because of the slightly different values for $N(\text{H I})$ and $N(J)$ for the H_2 compared to the earlier study of Wakker (2006) we here also update the subsequent determination

TABLE 2
SUMMARY OF GAS-PHASE ABUNDANCES AND DUST DEPLETION VALUES IN COMPONENTS 1+2

Ion X of element M	Z	I.P. ^a [eV]	$\log(M/H)_{\odot}^b$ +12	$\log(X/H I)^c$	I.C. ^d	[M/H] ^e	$\log \delta(M)^f$
C I	6	11.26	8.43 ± 0.05	-6.93 ± 0.07
N I	7	14.53	7.83 ± 0.05	-5.49 ± 0.09	-0.03	-1.31 ± 0.09	...
N II	7	14.53	7.83 ± 0.05	-6.26 ± 0.13
O I	8	13.62	8.69 ± 0.05	-3.90 ± 0.27	-0.01	-0.60 ± 0.27	...
Al II	13	18.83	6.45 ± 0.03	-7.29 ± 0.09	+0.03	-1.71 ± 0.09	-1.18
Si II	14	16.35	7.51 ± 0.03	-5.51 ± 0.09	-0.12	-1.00 ± 0.09	-0.61
P II	15	19.77	5.41 ± 0.04	-7.08 ± 0.09	+0.01	-0.48 ± 0.09	...
S II	16	23.34	7.12 ± 0.03	-5.41 ± 0.08	0.00	-0.53 ± 0.08	...
Ca II	20	11.87	6.34 ± 0.04	-8.22 ± 0.09	$\leq +1.35$	≥ -1.83	≥ -1.35
Fe II	26	16.12	7.50 ± 0.04	-5.99 ± 0.09	-0.09	-1.58 ± 0.09	≥ -1.05

^a I.P.= ionization potential.

^b Solar reference abundance for element M from Asplund et al. (2009).

^c Listed errors include uncertainties from the column-density measurements of X and H I.

^d I.C.= ionization correction, as defined in Sect. 4.1.

^e Gas phase abundance for element M, defined as $[M/H] = \log(M/H) - \log(M/H)_{\odot}$.

^f Depletion value, defined as $\log \delta(M) = [M/H]_{LA} - [S/H]_{LA}$.

of physical parameters in the H₂ gas, such as density, temperature, thermal pressure.

For the interpretation of the relative H₂ abundance and the analysis of the H₂ rotational excitation, we follow exactly the same strategy as described in R13. The most important equations are summarized in the Appendix.

If we balance the local UV flux in the LA II (based on the radiation model presented in Fox et al. 2014 assuming $d = 20$ kpc) with a SMC-type H₂ grain-formation rate (Tumlinson et al. 2002) and further assume that H₂ line-self shielding applies, we obtain $\phi n_H = 8 \text{ cm}^{-3}$. Here, $\phi \leq 1$ describes the column-density fraction of the H I in comp. 1 that is physically related to the H₂ absorbing gas (see Appendix for details). This density is roughly eight times higher than the density in the H₂ bearing clump in the LMC-filament of the MS (R13). Lacking any further information on the density distribution in comp. 1 we assume in the following $\phi = 0.5$ as a realistic value (see R13), so that we obtain $n_H = 16 \text{ cm}^{-3}$. From the 21 cm ATCA observations alone, WOP02 estimates (from geometrical considerations in the high-resolution interferometer data) a gas density of $n_H = 20 \text{ cm}^{-3}$ in the densest cloud cores, thus in excellent agreement with our value.

The thickness of the H₂ absorbing structure in the LA II then is given by $l_{H_2} = \phi N(H I) / n_H \approx 0.8 \text{ pc}$, which is tiny compared to the overall size of LA II as seen in 21 cm emission (kpc-scale at a distance of $d = 20$ kpc). Although the line of sight towards NGC 3783 passes LA II in a valley of the H I column-density distribution (Fig. 1), it obviously intersects a small, dense, dusty gas clump.

We now turn to the rotational excitation of the H₂, which provides important information on the local gas temperature in the cloud core (as in dense gas the lower rotational levels are excited by collisions). In Fig. 7 we show the H₂ column density for each rotational state, $\log N(J)$, divided by the state's statistical weight, g_J , against its excitation energy, E_J . The distribution of the data points can be fit for $J \leq 3$ with a single Boltzmann distribution with $T_{\text{kin}} \approx T_{\text{ex}} = (105 \pm 14) \text{ K}$, in Fig. 7 shown as dashed line. Within the error range, this temperature is similar to values typically found in IVCs, in

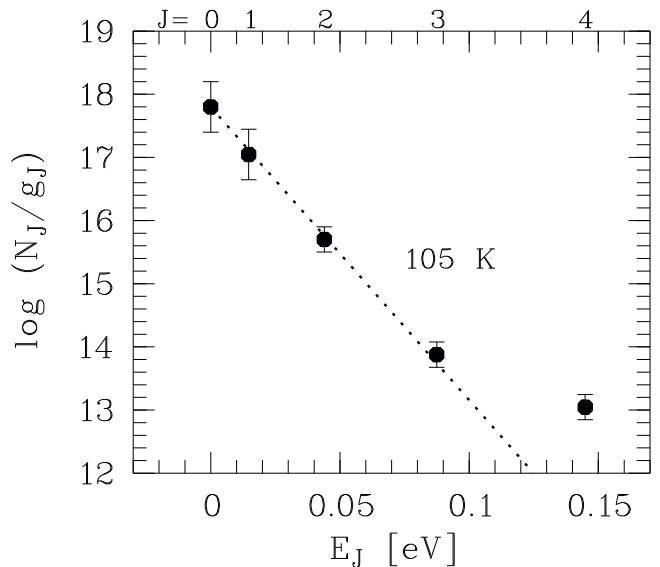


FIG. 7.— Rotational excitation of H₂ in the LA II. The H₂ column density for each rotational state, divided by the state's statistical weight, is plotted against the state's excitation energy. The data up to $J = 3$ fit a single-component Boltzmann distribution with an excitation temperature of $T_{\text{ex}} = (105 \pm 14) \text{ K}$.

the MS towards Fairall 9, and in the MCs (Richter 2000; Richter et al. 2003a; Wakker 2006; R13; Tumlinson et al. 2002), but is slightly higher than the canonical value of $T_{\text{kin}} = 77 \text{ K}$ that is characteristic for the MW disk (Savage et al. 1977). But while in H₂-absorbing environments in the MW and in the MCs a two-component Boltzmann fit usually is required to account for photon-pumping processes in the higher J levels ($J \geq 2$; e.g., Jura 1974), the H₂ rotational excitation in the LA II follows a different scheme with just a single-component fit for $J = 0-3$. This is not surprising, however, because the local UV radiation field in the LA II is expected to be by a factor ~ 35 lower compared to the MW disk (Fox et al. 2014) due to the absence of a *significant* (in terms of stellar luminosity density) local stellar population. Therefore, photon-pumping is not efficient in the LA II and the rotational excitation by collisions is the only relevant process

that governs the distribution of $N(J)$ from the ground states $J = 0, 1$ up to $J = 3$.

With R_{LA} as SMC H_2 grain-formation rate density (see Appendix), the H_2 formation-time scale in the LA II towards NGC 3783 is $(Rn_{\text{H}})^{-1} \approx 640$ Myr. Depending on the origin and age of LA II, the observed H_2 could be a relic of ancient molecule formation in the source galaxy of the LA, or it could have formed in situ, with f_{H_2} adjusting to the local physical conditions after the gas has been ripped off the stellar body. These aspects will be further discussed in Sect. 5.1.

With $T_{\text{kin}} = 105$ K and $n_{\text{H}} = 16 \text{ cm}^{-3}$, the thermal pressure in the LA II comes out to $P/k = n_{\text{H}}T = 1680 \text{ cm}^{-3} \text{ K}$ ($\log P/k = 3.23$; see also Wakker 2006). This is more than twice the pressure than what has been determined in the main body of the MS towards Fairall 9 (R13). This significant pressure difference most likely reflects the different locations of MS and LA in the halo with respect to the MW disk. With $d \leq 20$ kpc (Casetti-Dinescu et al. 2014; Zhang et al. 2017) the LA II is much closer to the disk than the main body of the MS, which is assumed to be at $d \approx 50 - 100$ kpc. From the models of Wolfire et al. (1995) it follows that a value of $\log P/k = 3.23$ for gas with an SMC chemical composition is above the thermal pressure component expected for a cold halo cloud located several kpc above/below the disk. If the ram pressure of the infalling high-velocity gas is included as an additional pressure component, however, the derived value for P/k in LA II is in line with the expectations. For a characteristic infall velocity of $v_{\text{infall}} = 150 \text{ km s}^{-1}$ (Heitsch & Putman 2009), a value of $\log P/k = 3.23$ corresponds to a vertical height above the plane of $z \approx 10$ kpc (see Fig. 5 in Wolfire et al. 1995), if a coronal gas temperature of $T = 1 - 2 \times 10^6$ K is assumed (Miller & Bregman 2015). This z height falls into the range expected from the observed stellar distances in LA II (Casetti-Dinescu et al. 2014, their Fig. 3). Therefore, it is plausible that the high gas density in the H_2 bearing clump and the resulting high value for P/k reflect the proximity of LA II to the Milky Way disk and its compression by the hydrodynamical interaction with the ambient coronal gas due to the high infall velocity. Similar arguments have been used to explain the observed extremely high thermal gas pressures in *out-flowing* gas in the lower Galactic halo that most likely is associated with the Milky Way nuclear wind (Savage et al. 2017). Unfortunately, a more precise estimate of the total gas pressure and the vertical position of LA II above the plane, which is highly desired to further explore the possible interaction of LA II with the Milky way disk (McClure-Griffiths et al. 2008), cannot be given at this point. This is because the ram pressure acting on the gas depends strongly on the space velocity of LA II, while only its radial velocity is securely constrained.

4.2. Fine-structure excitation of neutral and ionized carbon

4.2.1. Fine-structure excitation of C I

With an ionization potential of 11.2 eV, neutral carbon can exist in detectable amounts only in dense interstellar regions where a high recombination rate can compensate for the photoionization of C I. The detection of C I in comp. 1 (Table 1) indicates the presence of dense gas

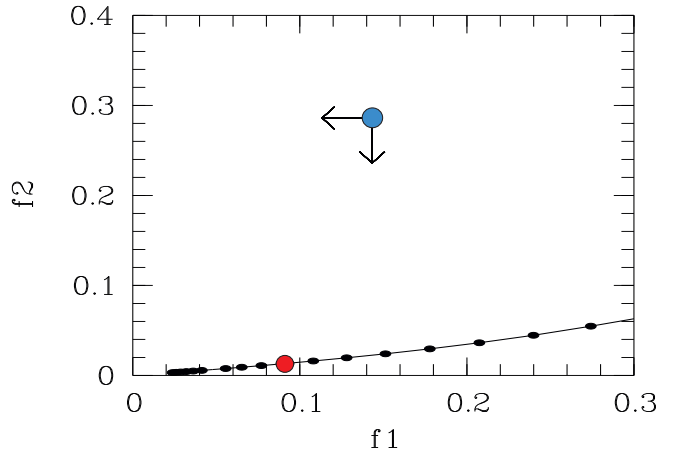


FIG. 8.— Limits on the relative abundances of the upper fine-structure levels of C I (parametrized by the quantities f_1 and f_2 ; see text) in LA II towards NGC 3783 (blue filled circle). The solid black line shows the collisionally excitation model for $T = 100$ K from Jenkins & Tripp (2001). The black dots on the line indicate increasing logarithmic gas densities (from left to right) in steps of 0.1 dex, while red solid point indicates the expected position for $\log n_{\text{H}} = 1.0$.

on its own, in line with above discussed gas properties derived from the H_2 absorption. The measurement of the C I in each of its three fine-structure levels (C I, C I*, C I**) further allows a direct (independent) measurement of the thermal pressure in the gas, as demonstrated in the local ISM (e.g., Jenkins & Tripp 2001). Absorption in C I* and C I** is not detected in LA II towards NGC 3783, but upper limits have been derived (see Table 1).

Following the strategy discussed in Jenkins & Tripp (2001) we define for the relative abundance of the upper fine-structure levels the parameters $f_1 = N(\text{C I}^*)/N(\text{C I}_{\text{tot}})$ and $f_2 = N(\text{C I}^{**})/N(\text{C I}_{\text{tot}})$. In Fig. 8 we plot f_1 vs. f_2 and compare the position of this single data point for LA II (blue filled circle) with the collisional excitation model for $T = 100$ K (solid line) from Jenkins & Tripp (2001; their Fig. 5). The black dots on the line indicate increasing logarithmic gas densities (from left to right) in steps of 0.1 dex. The red solid point indicates the position for $\log n_{\text{H}} = 1.0$. As can be seen, no useful constraints on the gas density/pressure in LA II can be obtained from the limits on C I* and C I**. However, since this is one of the very few HVCs for which this experiment can be carried out because of the very high S/N in the STIS data and the detection of C I, we show this diagnostic plot for sake of completeness (see also Savage et al. 2017 for another example)..

4.2.2. Fine-structure excitation of C II

Because the relative population of the fine-structure levels of ionized carbon (C+) are governed by the balance between collisions with electrons and the radiative decay of the upper level into the ground state, the column-density ratio between C II* and C II (or other singly ionized species) serves as measure for the electron density in different interstellar environments (including HVCs and other CGM structures; Zech et al. 2008; Jenkins et al. 2005). In our previous study of the main body of the MS we have used the C II*/S II ratio to determine the electron density in the Stream towards Fairall 9 and C II*/H I to estimate the local cooling rate in the gas

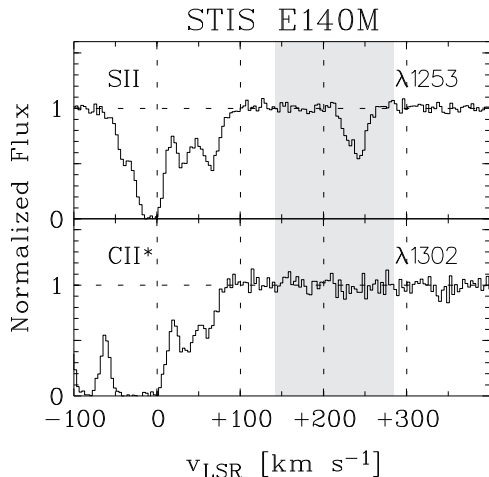


FIG. 9.— Velocity profile of $C\text{II}^*$ $\lambda 1335.7$ absorption (lower panel) compared to $S\text{II}$ $\lambda 1253$. The gray-shaded area indicates the velocity range in which absorption from LA II is expected. No significant $C\text{II}^*$ absorption is detected, however.

(R13).

In Fig. 9 we compare the velocity profile of $C\text{II}^*$ $\lambda 1335$ and $S\text{II}$ $\lambda 1253$ in our STIS spectrum of NGC 3783. No significant $C\text{II}^*$ $\lambda 1335$ absorption is detected at LA II velocities (gray-shaded) range, but a significant upper limit of $\log N(C\text{II}^*) \leq 12.93$ can be measured from the data. Following the strategy outlined in R13, we estimate from the measured column-density ratio $\log [N(C\text{II}^*)/N(S\text{II})] \leq -1.47$ in comp. 1 that $\log [N(C\text{II}^*)/N(C\text{II})] \leq -2.78$ (assuming a solar S/C ratio in the gas). For $T \approx 100$ K, (as measured from the H_2 rotational excitation), this is a very low value and only reproducible in $C\text{II}$ fine-structure population models if the *average* gas density in comp. 1 is by a factor of $\sim 5 - 10$ smaller than the peak value of $n_{\text{H}} = 16 \text{ cm}^{-3}$ seen in the H_2 -absorbing gas clump (see Keenan et al. 1986; their Fig. 2). In any case, the upper limit for the electron density in comp. 1 is $n_e = 0.01 \text{ cm}^{-3}$ (Keenan et al. 1986), a value that is characteristic for cold neutral gas at low metallicities (e.g., Wolfire et al. 1995) and comparable to what has been found in the MS towards Fairall 9 ($n_e \leq 0.05 \text{ cm}^{-3}$; R13).

As mentioned above, the $C\text{II}^*/\text{HI}$ ratio in LA II can be used to estimate the local C^+ cooling rate, which is governed predominantly by spontaneous de-excitations at these densities (Spitzer 1978). Following Lehner et al. (2004), the C^+ cooling rate per hydrogen atom can be calculated via the relation $l_C = 2.89 \times 10^{-20} N(C\text{II}^*)/N(\text{HI}) \text{ erg s}^{-1}$. For LA II, we derive as sightline average (integrating over all velocity components) an upper limit of $\log l_C \leq -26.62$. This value lies between the one derived for the HVC Complex C (≈ 0.15 solar abundance, $\log l_C \approx -27$; Lehner et al. 2004; Richter et al. 2001) and the main body of the MS towards Fairall 9 (0.5 solar abundance, $\log l_C \approx -26$; R13), which is not surprising given the fact that LA II has a metallicity of 0.3 solar.

5. DISCUSSION

Our study confirms earlier results on the global metal abundance of LA II (Lu et al. 1998; Fox et al. 2018) and provides new information on the dust properties and physical conditions in the gas, further constraining of

the origin of the LA and its evolution.

5.1. Physical properties and small-scale structure

Taken together, the STIS, FUSE, and ATCA data indicate that the gas in LA II in front of NGC 3783 is multiphase, with several low-density components and two dense, neutral cloud cores at $v_{\text{LSR}} = 245$ and 179 km s^{-1} (see Table 1). Comp. 1, in particular, exhibits properties that are remarkable for a Galactic halo cloud, with a very high gas density of $\sim 16 \text{ cm}^{-3}$, a low gas temperature of $T = 105 \text{ K}$, resulting in a high thermal pressure of $P/k \approx 1680 \text{ K cm}^{-3}$, and a relatively high molecular gas fraction. These results are in line with previous observations and consistent with the detection of a stellar population in LA II (Casetti-Dinescu et al. 2014), indicating that LA II is situated at a distance of $d < 20$ kpc relatively close to the disk ($z \approx 10$ kpc), where the gas is compressed and disrupted by ram pressure forces as a result of the interaction with the ambient hot halo gas. The physical properties and infall/disruption timescales mimic those seen in hydrodynamical simulations of cold gas clouds moving into a hot plasma at high speed (e.g., Heitsch & Putman 2009; Joung et al. 2012; Tepper-García et al. 2015; Armilotta et al. 2016).

The H_2 bearing clump within LA II has a linear size of only 0.8 pc (see Sect. 4.1), reflecting the clumpiness of the fragmenting neutral gas body of LA II. But also comp. 3 at $+179 \text{ km s}^{-1}$ appears to have a surprisingly high gas density of $n_{\text{H}} \geq 0.3 \text{ cm}^{-3}$ (Sect. 3.4.3), which translates to an absorber thickness of just $l = N(\text{HI})/n_{\text{H}} \leq 6$ pc, thus very small as well. The formation of tiny, dense gas clumps due to the ablation of large neutral gas complexes appears to be a phenomenon that is characteristic for the hydrodynamical interaction between infalling gas clouds and the ambient hot coronal gas, as similar features have been observed also in other HVC complexes (see Richter et al. 2003b, 2005b, 2009).

5.2. Dust abundance

One aspect that deserves further attention is the very high dust abundance seen in LA II towards NGC 3783 in both absorber groups. With the large depletion values of $\delta(\text{Si}) = -0.5$ to -0.6 dex, $\delta(\text{Fe}) \geq -1.1$ dex, $\delta(\text{Al}) = -1.2$ dex, and $\delta(\text{Ca}) \geq -1.4$ dex the dust content is exceptionally high for the low metallicity and the moderate neutral+molecular gas column density of $\log N(\text{H}) \approx 20$. To put these results into a context, we compare the observed depletion values with those found in the LMC and SMC. Tchernyshyov et al. (2015) and Jenkins & Wallerstein (2017) recently have studied the depletion properties of various different elements in the LMC and SMC using UV absorption-line data from HST/COS, HST/STIS, and FUSE. In their studies, depletion values as high as in LA II are found in the LMC and SMC only in regions with total gas columns that are *substantially* higher than in the LA II towards NGC 3783.

To demonstrate this, we show in Fig. 10 the Si depletion, $\delta(\text{Si})$, in comp. 1+2 and comp. 3 as a function of the total neutral+molecular hydrogen column density, $\log N(\text{H})$, for LMC, SMC, and LA II, based on the results of Tchernyshyov et al. (2015) and this study. The Si depletion value in LMC and SMC increases strongly for decreasing hydrogen gas column densities, as evident

from the fits to the LMC and SMC data (solid red and blue lines in Fig. 6.) This overall trend is well known from observations in the Milky Way and interstellar environments in other galaxies (Jenkins 2009), where the horizontal position of the data points scales with the dust-to-gas ratio. Obviously, the measured dust depletion in LA II towards NGC 3783 in comp. 1+2 and comp. 3 does not fit to the depletion trends in either LMC or SMC: it is apparently too strong for the relatively low neutral+molecular hydrogen column density, indicating a strongly enhanced local dust-to-gas ratio. Fig. 10, indicates that the level of depletion observed in LA II at $\log N(\text{H}) = 18.7$ and $\log N(\text{H}) = 20.0$ would correspond to a total neutral+molecular hydrogen column as high as $\log N(\text{H}) \approx 21.2$ in the SMC (filled yellow box in Fig. 10), with both environments having the same metallicity and overall abundance pattern.

There are two opposite ways to interpret this interesting deviation: either, LA II has an unusually high fraction of heavy elements depleted into dust grains when compared to LMC and SMC gas, or, for a given amount of dust, there is locally a reduced neutral+molecular gas column density in LA II along the NGC 3783 sightline (or a combination of both effects). We discuss both of these scenarios in the following.

Enhanced dust growth. Because most of the depletion of heavy elements into dust grains occurs due to dust growth in the dense interstellar medium (e.g., Draine 2009; Jenkins et al. 2009), it may well be possible that the large dust-to-gas ratio in LA II reflects an efficient dust growth *in situ*, possibly favoured by the high local gas density in comp. 1 and 3 and the absence of stellar and supernovae feedback that would lead to dust destruction. It still appears remarkable (and not completely convincing to us) that even in dense CGM environments the dust growth is so extremely efficient that a disk-like dust abundance is achieved at column densities that are only a few percent of those observed in disks.

Reduction of gas column density. In this scenario, the neutral+molecular gas column density was substantially reduced (e.g., through hydrodynamical interaction with the ambient hot coronal gas) after the gas was ripped off its mother galaxy, while the initial amount of dust stayed constant (or even was increased, see above scenario). If so, the stripped gas in LA II would have “stored” the initial SMC/LMC-type relative dust abundance/depletion value (Fig. 10), while the infalling cloud was breaking up and fragmenting into sub-clumps with a substantially reduced total neutral+molecular gas column density (see Heitsch & Putman 2009; Tepper-García et al. 2015). Note that the dust-destruction timescale in the CGM far from any supernova shocks and intense UV radiation fields is expected to be very long, possibly a few 10^8 yr (Draine & Salpeter 1979).

The 21 cm map shown in Fig. 1 does indeed demonstrate that the NGC 3783 sightline passes a *minimum* in the H I column-density (CD) distribution of LA II, lying between several clumps of higher CD (up to $\log N(\text{H I}) = 20.6$; WOP02). If the observed depletion level in LA II towards NGC 3783 reflects the initial dust conditions of the gas at the time when it was separated from the MCs, then the logarithmic neutral+molecular hydrogen column has dropped from ~ 21.2 to ~ 20.0 (comp. 1+2+3; see Fig. 10) along this sightline, as the

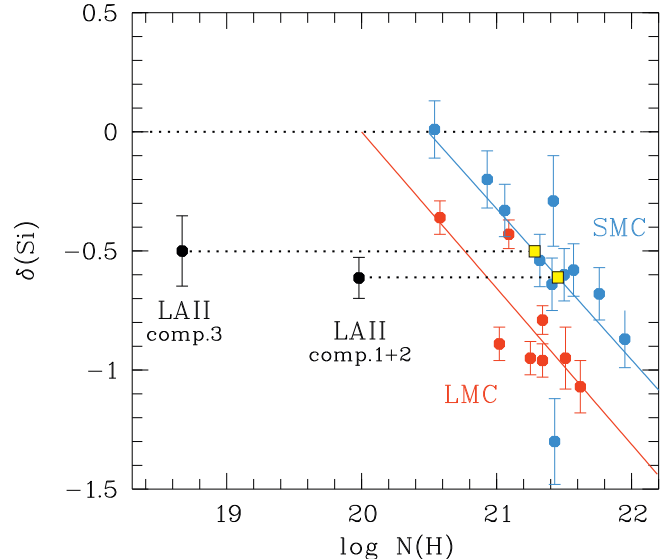


FIG. 10.— Si depletion values, $\delta(\text{Si})$, for LMC gas (filled red circles), SMC gas (blue filled circles), and for LA II (filled black circles) in comp. 1+2 and comp. 3 as function of the total atomic+molecular hydrogen column density. LMC and SMC data are adopted from Tchernyshyov et al. (2015). The filled yellow box marks the hypothetical initial position of LA II for the cloud-disruption model discussed in Sect. 5.2.

cloud has moved into the inner Milky Way halo. This is a reduction by more than 95 percent in neutral+molecular gas column. Given the long pathlength and the high radial velocity, such a cloud break-up and ablation of neutral gas column is actually expected from hydrodynamical simulations that model the properties of neutral gas clouds of different initial masses as they move at high speed through an ambient hot medium (Heitsch & Putman 2009; Joung et al. 2012; Tepper-García et al. 2015).

While we here can only speculate about the origin of the high dust-to-gas ratio in LA II, it represents a remarkable feature that deserves further attention in future studies. Interestingly, previous analyses of the strongly depleted element Ca have demonstrated that dust commonly reaches out far beyond the stellar bodies of galaxies deep into circumgalactic and intergalactic space (e.g., Zhu & Ménard 2013; Richter et al. 2011). In this broader context, additional systematic studies of metal depletion in the Milky Way halo and in other circumgalactic environments would be very useful to better understand the large-scale circulation of dust in and around galaxies.

5.3. Origin of LA II

To further evaluate whether LA II originally stems from the SMC or LMC let us first collect the main results from our absorption-line study and summarize the main conclusions from these findings:

1. LA II exhibits an α abundance and N/α ratio that closely matches that of the current-day SMC, possibly implying that the gas recently was removed from the SMC and pushed deep into the Milky Way halo. If so, the age of LA II can be at most a few hundred Myr. If we consider only the chemical abundance pattern as age indicator, LA II could be older if the gas originates in the LMC. In that case, the observed abundance pattern in LA II would re-

fect that of the LMC 1-2 Gyr ago (Pagel & Tautvaivsiene 1998; Harris & Zaritsky 2004). That the LMC had *exactly* the same α/N abundance pattern as the SMC today at the time when the gas was removed from the MCs is not unrealistic given the star-formation history of the LMC (Pagel & Tautvaivsiene 1998), but it would be a coincidence.

2. LA II exhibits a very high thermal gas pressure of $P/k \approx 1680 \text{ K cm}^{-3}$ in the molecular gas-phase, suggesting that the gas is situated in the *inner* halo of the Milky Way $\approx 10 \text{ kpc}$ above the disk, where the gas is compressed by ram-pressure forces. LA II and the MCs then would be separated by at least 30 kpc in space, suggesting that it would have taken the gas more than 200 Myr to reach its current position after it was separated from its host galaxy (assuming a relative speed of 100 km s^{-1}). This sets a minimum age of $\sim 200 \text{ Myr}$ to the LA II. Yet, a distance as small as 10 kpc for the LA cannot be reproduced by the most recent hydrodynamical simulations of the Magellanic System (Pardy et al. 2018) in a first infall scenario, where the minimum distance of the LA is found to be $d \approx 24 \text{ kpc}$.
3. The H_2 formation time-scale in the cold gas in LA II is $\sim 640 \text{ Myr}$. If all of the H_2 had formed in situ, this sets a lower limit for the age of the LA II. However, given the fact that so much dust has survived the separation process, it is equally likely that also the H_2 (or at least part of it) had formed earlier in the LA II source galaxy. If so, the H_2 was transported together with the neutral gas into the Milky Way halo, where the molecular gas fraction adjusted to the local conditions on much smaller time scales.
4. The very high dust-to-gas ratio in LA II suggests that the gas originally stems from a interstellar region with a neutral+molecular gas column as high as $\log N(\text{H}) = 21.2$. Such high column densities are typical for the inner region in both LMC and SMC (see, e.g., Brüns et al. 2005; their Fig. 5), but the average and peak HI column density is higher in the SMC than in the LMC. The high dust content in LA II strongly suggests that the gas was removed “calmly” from the MCs by ram-pressure forces and/or tidal forces, but not by “violent” processes, such energetic outflows from star-bursting regions that would have destroyed most of the dust (Feldmann 2015).

In summary, the observed chemical and physical properties do not exclude an LMC origin of LA II, but they favor an SMC origin. In the latter case, the gas in LA II was removed from the SMC 200 – 500 Myr ago during a close LMC-SMC encounter (Besla et al. 2012; Hammer et al. 2015; Pardy et al. 2018), followed by a rapid decent into the Milky Way halo where the gas cloud was breaking up and fragmented into smaller pieces due to the hydrodynamical interaction with the hot coronal gas.

If we combine the results from this study with those obtained from our recent HST/COS survey of the LA

(Fox et al. 2018) we find that there is a substantial metallicity/age spread within the LA. The lowest metallicity ($\sim 0.04 - 0.06$ solar) is found in LA III, followed by LA I, which has ~ 0.12 solar abundance, thus very similar to that in the main body of the MS (Fox et al. 2013). In contrast, the metallicity in LA II, as measured here, is with ~ 0.3 solar substantially higher than in the other LA complexes. Yet, it is still only half of that measured in the LMC filament of the MS (R13). As discussed in Fox et al. (2018), the observed metallicity spread in the LA most likely indicates an episodic removal of gas from the SMC, with LA III being the oldest part stripped from the SMC together with the main body of the MS 1 – 2 Gyr ago, followed by the later removal of LA I and LA II due to more recent encounters of SMC and LMC. Our abundance measurements therefore set important new constraints for the numerical modeling of the the Magellanic System (see Pardy et al. 2018). A detailed and systematic comparison between the observational results and the results from the numerical simulations would be of great importance to better understand, how the various components of the MS and LA came to their existence and what the observed gas properties tell us about the formation of the Magellanic System.

One other aspect that needs further attention in future LA studies is the role of the LA’s recently detected stellar population for the physical and chemical properties of the gas (Casetti-Dinescu et al. 2014; Zhang et al. 2017). While stars within the LA generally must lead to a local self-enrichment that may have the potential to also increase the metal and dust abundance in the gas on larger spatial scales, it remains to be evaluated in detail, how relevant this effect could be and whether the observed abundance variations in the LA could be related to such a local stellar population.

6. SUMMARY AND CONCLUSIONS

In this paper, we have presented new results on the chemical composition of the Leading Arm of the Magellanic Stream in the direction to the Seyfert galaxy NGC 3783, based on the combination of archival spectral data from HST/STIS, FUSE, ATCA, GBT, and other instruments. Our main results can be summarized as follows:

1. Six individual velocity components belonging to LA II are identified in the high-resolution STIS data at radial velocities between +179 and +269 km s^{-1} . There are two main absorber groups located at +190 and +245 km^{-1} that give rise to emission seen in the 21 cm data. From the STIS data we construct an absorption-component model that we apply also to the lower-resolution FUSE and ATCA 21 cm emission data.
2. From the modeling of the S II , O I , and P II absorption lines in the STIS data and the analysis of the 21 cm data from ATCA and GBT we determine in both absorber groups a common α abundance in LA II of $[\alpha/\text{H}] = -0.53 \pm 0.08$, corresponding to 0.30 ± 0.05 solar. This estimate includes an ionization correction based on *Cloudy* photoionization models of the gas in LA II. This value is similar to the present-day stellar α abundance in the SMC.

Our results confirm previous estimates of the LA II abundance based on low-resolution spectral data (Lu et al. 1998), but increases substantially the significance of this finding.

3. For the first time, we measure the abundance of nitrogen in the LA. The N abundance in LA II is very low, $[N/H] = -1.31 \pm 0.09$ (0.05 ± 0.01 solar) and $[N/\alpha] = -0.78$, again matching closely the present-day photospheric nitrogen abundance in the SMC. The elements Si, Fe, Al, and Ca are substantially depleted into dust grains. We determine depletion values of $\delta(\text{Si}) = -0.5$ to -0.6 dex, $\delta(\text{Fe}) \geq -1.1$ dex, $\delta(\text{Al}) = -1.2$ dex, and $\delta(\text{Ca}) \geq -1.4$ dex. The substantial depletion values indicate that the local dust-to-gas ratio is very high for the only moderate HI columns $\log N(\text{HI}) < 20$ in both main absorber groups. We compare these values with depletion patterns in LMC and SMC gas (Tchernyshyov et al. 2015) and conclude that the gas in LA II presumably stems from a region that initially had a high gas column density of $\log N(\text{H}) \approx 21.2$.
4. The re-analysis of the H₂ absorption in the FUSE data yields column densities for the rotational levels, $N(J)$, that are very similar to those found in Wakker (2006). With a total H₂ column density of $\log N(\text{H}_2) = 18.22$ the molecular fraction in the gas is 0.04, which is (like the dust abundance) surprisingly high for the moderate HI column density. We model the H₂ abundance in a formation-dissociation equilibrium including H₂ self-shielding and a dissociating UV flux appropriate for the position of LA II in the Milky Way halo. From this we derive a high gas density of $n_{\text{H}} = 16 \text{ cm}^{-3}$ in the cloud core of LA II. The rotational excitation of the H₂ yields a kinetic gas temperature of $T_{\text{kin}} = (105 \pm 14) \text{ K}$, implying that the thermal pressure in the molecular gas is as high as $P/k \approx 1680 \text{ K cm}^{-3}$.
5. The fact that the absolute and relative metal abundances in LA II exactly match those observed in the SMC stellar population supports the scenario, in which LA II was stripped from the SMC during a recent LMC-SMC encounter 200 – 500 Myr ago. However, an LMC origin as part of an earlier stripping process cannot be completely excluded from our data set. The overall abundance spread in the LA presented in Fox et al. (2018), with LA II being the most metal-rich region, points toward a periodic removal of gas from the SMC, forming the chain of LA complexes seen today. The physical conditions in LA II and the high dust abundance, as derived in this study, indicate that the gas originally was of much higher column density before it was sinking into the Milky Way halo and being disrupted and dissolved due to the interaction with the ambient hot halo gas. The high gas pressure in LA II suggests that LA II is only ≈ 10 kpc away from the disk of the Milky Way in the lower halo or disk-halo interface, where ram-pressure forces add significantly to the overall pressure budget on in-falling neutral gas clouds.

This work is based on observations with the NASA/ESA Hubble Space Telescope, obtained at the Space Telescope Science Institute (STScI), which is operated by the Association of Universities for Research in Astronomy, Inc., under NASA contract NAS 5-26555. Spectra were retrieved from the Barbara A. Mikulski Archive for Space Telescopes (MAST) at STScI. BPW was supported by NASA grants HST-GO-13448.01-A and HST-AR-14577.01-A. JCH and NL recognize support for this work from NASA and the NSF through grants HST-GO-14602 and AST-1517353, respectively. ED gratefully acknowledges the hospitality of the Center for Computational Astrophysics at the Flatiron Institute during the completion of this work.

REFERENCES

- Abgrall, H., & Roueff, E. 1989, *A&A*, 79, 313
- Armilotta, L., Fraternali, F., & Marinacci, F. 2016, *MNRAS*, 462, 4157
- Asplund, M., Grevesse, N., Jacques Sauval, A., & Scott, P. 2009, *ARA&A*, 47, 481
- Barger, K.A., Haffner, L.M., & Bland-Hawthorn, J. 2013 *ApJ*, 771, 132
- Barger, K.A., Madsen, G.J., Fox, A.J., et al. 2017, *ApJ*, 851, 110
- Besla, G., Kallivayalil, N., Hernquist, L., et al. 2010, *ApJL*, 721, L97
- Besla, G., Kallivayalil, N., Hernquist, L., et al. 2012, *MNRAS*, 421, 2109
- Boothroyd, A.I., Blagrove, K., Lockman, F.J., et al. 2011, *A&A*, 536, A81
- Brown, T., et al. 2002, *HST STIS Data Handbook*, v.4, ed. B. Mobasher (Baltimore: STScI)
- Brüns, C., Kerp, J., Staveley-Smith, L., et al. 2005, *A&A*, 432, 45
- Bustard, C., Pardy, S.A., D’Onghia, E., Zweibel, E.G., & Gallagher, J.S.III 2018, *ApJ*, in press
- Casetti-Dinescu, Moni Bidin, C., K., Girard, T.M., et al. 2014, *ApJL*, 784, L37
- Dickey, J.M. & Lockman, F.J. 1990, *ARA&A*, 28, 215
- D’Onghia, E., & Fox, A.J. 2016, *ARA&A*, 54, 363
- Draine, B. & Salpeter, E.E. 1979, *ApJ*, 231, 438
- Draine, B., & Bertoldi, F. 1996, *ApJ*, 468, 269
- Draine, B. 2009, *ASPC*, 414, 453
- Feldmann, R. 2015, *MNRAS*, 449, 3274
- Ferland, G. J., Porter, R. L., van Hoof, P. A. M., et al. 2013, *RMxAA*, 49, 137
- For, B.-Q., Staveley-Smith, L., McClure-Griffiths, N.M., Westmeier, T., & Bekki, K. 2016, *MNRAS*, 461, 892
- Fox, A.J., Wakker, B.P., Smoker, J.V., et al. 2010, *ApJ*, 718, 1046
- Fox, A.J., Richter, P., Wakker, B.P. et al. 2013, *ApJ*, 772, 110
- Fox, A.J., Richter, P., Barger, K.A., et al. 2014, *ApJ*, 787, 147
- Fox, Anne, Richter, P., & Fechner, C. 2014, *A&A* 572, A102
- Fox, A.J., Barger, K.A., Wakker, B.P., et al. 2018, *ApJ*, 854, 142
- Gabel, J.R., Crenshaw, D.M., Kraemer, S.B., et al. 2003a, *ApJ*, 583, 178
- Gabel, J.R., Crenshaw, D.M., Kraemer, S.B., et al. 2003b, *ApJ*, 595, 120
- Hammer, F., Yang, Y.B., Flores, H., Puech, M., & Fouquet, S. 2015, *ApJ*, 813, 110
- Harris, J., Zaritsky, D. 2004, *AJ*, 127, 1531
- Heitsch, F. & Putman, M. E. 2009, *ApJ*, 698, 1485
- Herenz, P., Richter, P., Charlton, J.C., & Masiero, J.R. 2013, *A&A*, 550, A87
- Howk, L.C., Wolfe, A.M. & Prochaska, J.X. 2005, *ApJL*, 622, L81
- Jenkins, E.B. & Tripp, T.M. 2001, *ApJS*, 137, 297

- Jenkins, E.B., Bowen, D.V., Tripp, T.M., & Sembach, K.R. 2005, *ApJ*, 623, 767
- Jenkins, E.B. 2009, *ApJ*, 700, 1299
- Jenkins, E.B. & Wallerstein, G. 2017, *ApJ*, 838, 85
- Joung, M.R., Bryan, G.L., & Putman, M.E. 2012, *ApJ*, 745, 148
- Jura, M. 1974, *ApJ*, 191, 375
- Keenan, F.P., Lennon, D.J., Johnson, C.T., & Kingston, A.E. 1986, *MNRAS*, 220, 571
- Lehner, N., Wakker, B.P., & Savage, B.D. 2004, *ApJ*, 615, 767
- Liang, C.J., & Chen, H.-W. 2014, *MNRAS*, 445, 2061
- Lu, L., Savage, B.D., & Sembach, K.R. 1994, *ApJ*, 437, L119
- Lu, L., Savage, B.D., Sembach, K.R., et al. 1998, *AJ*, 115, 162
- Mathewson, D. S., Cleary, M.N., & Murray, J.D. 1974, *ApJ*, 190, 291
- McClure-Griffiths, N.M., Staveley-Smith, L., Lockman, F.J. et al. 2008, *ApJ*, 673, L143
- Miller, M.J., & Bregman, J.N. 2015, *ApJ*, 800, 14
- Morton, D. C. 2003, *ApJS*, 149, 205
- Muzahid, S., Fonseca, G., Roberts, A., et al. 2018, *MNRAS*, 476, 4965
- Narayanan, A., Charlton, J.C., Masiero, J.R., & Lynch, R. 2005, *ApJ*, 632, 92
- Nidever, D. L., Majewski, S. R., & Burton, W. B. 2008, *ApJ*, 679, 432
- Nidever, D. L., Majewski, S. R., Burton, W. B., & Nigra, L. 2010, *ApJ*, 723, 1618
- Pardy, S.A., D’Onghia, E., & Fox, A.J. 2018, *ApJ*, 857, 101
- Pagel, B. E. J., & Tautvaisiene, G. 1998, *MNRAS*, 299, 535
- Petitjean, P., Ledoux, C., Srianand, R. 2008, *A&A*, 480, 349
- Pettini, M., Zych, B. J., Steidel, C. C., & Chaffee, F. H. 2008, *MNRAS*, 385, 2011
- Putman, M. E., Gibson, B. K., Staveley-Smith, L., et al. 1998, *Nature*, 394, 752
- Putman, M. E., Peek, J. E. G., & Joung, M. R. 2012, *ARA&A*, 50, 491
- Richter, P. 2000, *A&A*, 359, 1111
- Richter, P., Savage, B. D., Wakker, B. P., Sembach, K. R., & Kalberla, P. M. W. 2001, *ApJ*, 549, 281
- Richter P., Wakker B. P., Savage B. D., & Sembach K. R. 2003a, *ApJ*, 586, 230
- Richter, P., Sembach, K.R., & Howk, J.C. 2003b, *A&A*, 405, 1013
- Richter, P., Ledoux, C., Petitjean, P., & Bergeron, J. 2005a, *A&A*, 440, 819
- Richter, P., Westmeier, T., & Brüns 2005b, *A&A*, 442, L49
- Richter, P. 2006, *Rev. Mod. Astron.*, 19, 31
- Richter, P., Charlton, J.C., Fangano, A.P.M., Ben Bekhti, N., & Masiero, J.R. 2009, *ApJ*, 695, 1631
- Richter, P., Krause, F., Fechner, C., Charlton, J.C., & Murphy, M.T. 2011, *A&A*, 528, A12
- Richter, P., Fox, A.J., Wakker, B.P., et al. 2013, *ApJ*, 772, 111
- Richter, P., Wakker, B.P., Fechner, C., Herenz, P., Tepper-García, T., & Fox, A.J. 2016, *A&A*, 590, A68
- Richter, P., Nuza, S. E., Fox, A. J., et al. 2017, *A&A*, 607, A48
- Richter, P. 2017, *ASSL*, 430, 15
- Savage, B.D., Drake, J.F., Budich, W., & Bohlin, R.C. 1977, *ApJ*, 216, 291
- Savage, B.D. & Sembach, K.R. 1991, *ApJ*, 379, 245
- Savage, B.D. & Sembach, K.R. 1996, *ARA&A*, 34, 279
- Savage, B.D., Kim, T.-S., Fox, A.J., et al. 2017, *ApJ*, 232, 25
- Sembach, K.R., Howk, J.C., Savage, B.D., & Shull, J.M. 2001, *AJ*, 121, 992
- Spitzer, L. 1978, *Physical processes in the interstellar medium*, (New York Wiley-Interscience)
- Stocke, J.T. Keeney, B.A., Danforth, C.W., et al. 2014, *ApJ*, 791, 128
- Tchernyshyov, K., Meixner, M., Seale, J., et al. 2015, *ApJ*, 811, 78
- Tepper-García, T., Bland-Hawthorn, J., & Sutherland, R.S. 2015, *ApJ*, 813, 94
- Tsujimoto, T., Nomoto, K., Yoshii, Y., et al. 1995, *MNRAS*, 277, 945
- Tumlinson, J., Shull, J. M., Rachford, B. L., et al. 2002, *ApJ*, 566, 857
- Venzmer, M.S., Kerp, J., & Kalberla, P.M.W. 2012, *A&A*, 547, 12
- Wakker, B. P., Oosterloo, T. A., & Putman, M. E. 2002, *AJ*, 123, 1953
- Wakker, B.P. 2006, *ApJS*, 163, 282
- Wannier, P., & Wrixon, G. T. 1972, *ApJ*, 173, L119
- Werk, J.K., Prochaska, J.X., Thom, C., et al. *ApJS*, 2014, 17
- West, K.A., Pettini, M., Penston, M.V., Blades, J.C., & Morton, D.C. 1985, *MNRAS*, 215, 481
- Wolfire, M.G., McKee, C F., Hollenbach, D., & Tielens, A.G.G.M. 1995, *ApJ*, 453, 673
- Zech, W.F., Lehner, N., Howk, J.C., Dixon, W.V.D., & Brown, T.M. 2008, *ApJ*, 679, 460
- Zhang, L., Moni Bidin, C., Casetti-Dinescu, D.I., et al. 2017, *ApJ*, 835, 285
- Zhu, G. & Ménard, B. 2013, *ApJ*, 773, 16

APPENDIX
H₂ ANALYSIS

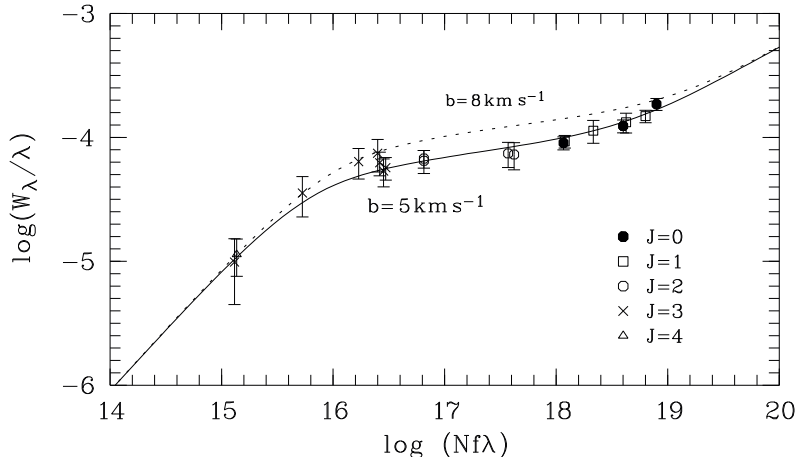


FIG. 11.— Curves of growth for H₂ absorption in comp. 1. The absorption lines arising from the rotational levels $J = 0 - 2$ fit best on a curve of growth with $b = 5.0 \text{ km s}^{-1}$. For $J = 3$, the scatter of the data points also allow higher b -values in the range $b = 5 - 8 \text{ km s}^{-1}$.

Curve-of-growth

To independently constrain the b -value for the H₂ absorption in the LA II we have measured the equivalent widths for a sub-set of unblended H₂ lines that have particularly high S/N in the FUSE data and constructed curves of growth (CoG; Fig. A.1). As can be seen, the CoG method further supports a b value of $b = 5.0 \text{ km s}^{-1}$ for the H₂, at least for the lower rotational levels $J = 0 - 2$. For $J = 3$, the scatter in the data points is larger than for $J \leq 2$, so that any value in the range $b = 5.0 - 8.0 \text{ km s}^{-1}$ is possible. If $b > 5.0 \text{ km s}^{-1}$ for $J = 3$, this would indicate that the rotationally excited H₂ gas is spatially more extended than the ground-state H₂, which is plausible within the scenario of a core-envelope structure of comp. 1. For the determination of the $J = 3$ column density, the choice of b within the range $b = 5.0 - 8.0 \text{ km s}^{-1}$ is not important, as $N(3)$ is constrained mostly by the very weak lines on the linear part of the CoG.

H₂ diagnostics

For the analysis of the H₂ absorption we follow the same strategy as adopted for the H₂ absorption in the main body of the MS towards Fairall 9 (R13). The relative abundance of H₂ compared to H I is regulated by the formation-dissociation equilibrium of molecular hydrogen, which can be expressed as

$$\frac{N(\text{H I})}{N(\text{H}_2)} = \frac{\langle k \rangle \beta}{R n(\text{H I}) \phi}. \quad (\text{A1})$$

In this equation, $\langle k \rangle \approx 0.11$ is the probability that the molecule is dissociated after photo absorption. The parameter $\phi \leq 1$ in equation (A1) describes the column-density fraction of the H I that is physically related to the H₂ absorbing gas, i.e., the fraction of neutral gas atoms that can be transformed into H₂ molecules (see Richter et al. 2003a for details).

The parameter β is the H₂ photo-absorption rate per second within the H₂-bearing cloud, while R represents the H₂ formation rate on dust grains in units $\text{cm}^3 \text{ s}^{-1}$. Estimating β for the LA is non-trivial, because one needs to estimate the dissociating photon flux at the position of the LA in the halo and, additionally, consider the effect of H₂ line-self shielding *within* the cloud. From the radiation-field model by Fox et al. (2014) it follows that the FUV photon flux at the position of the LA in the halo at distance 20 kpc is reduced by a factor of 35. For the H₂ photo-absorption rate in the Milky Way disk, we assume the canonical value of $\beta_{0,\text{MW}} = 5.0 \times 10^{-10} \text{ s}^{-1}$ (e.g., Spitzer 1978), which implies that $\beta_{0,\text{LA}} = 1.4 \times 10^{-11} \text{ s}^{-1}$ at the edge of the clump in the LA towards NGC 3783. The H₂ line-self shielding further reduces this absorption rate in the interior of the clump. Following the parametrization scheme presented by Draine & Bertoldi (1996), the absorption rate in the cloud can be expressed as $\beta = S \beta_0$, where $S = (N_{\text{H}_2}/10^{14} \text{ cm}^{-2})^{-0.75} < 1$. From this we finally obtain $\beta = 1.0 \times 10^{-14} \text{ s}^{-1}$ in the self-shielded cloud core.

The formation of H₂ predominantly takes place on the surface of dust grains, as pure gas-phase reactions of hydrogen atoms and ions are far less efficient than the formation on dust (e.g., Spitzer 1978). For the required H₂ grain formation rate in the LA, we adopt the value determined for the SMC (see Tumlinson et al. 2002), $R_{\text{LA}} = 3 \times 10^{-18} \text{ cm}^3 \text{ s}^{-1}$, which is appropriate given the SMC-like chemical abundance pattern in LA II and the observed dust-depletion pattern (Sect. 3.6). From equation (A1) we then derive $\phi n_{\text{H}} \approx 8 \text{ cm}^{-3}$.

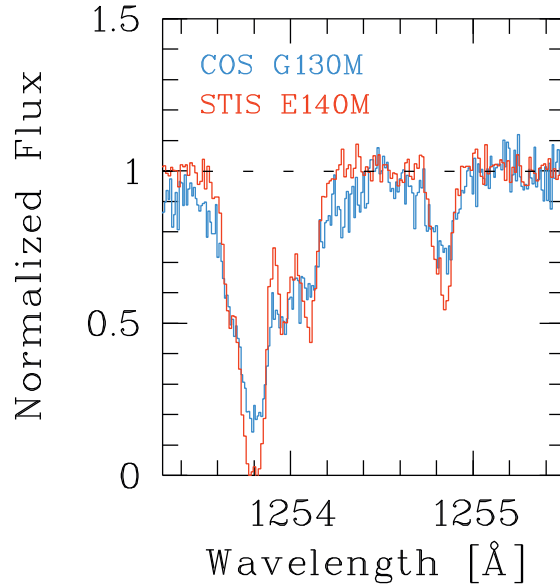


FIG. 12.— Comparison between STIS E140M data (red) and COS G130M data (blue) of NGC 3783 in the wavelength range between 1253.3 and 1255.5 Å, covering the S II λ 1253 line.

COMPARISON BETWEEN HST/STIS AND HST/COS DATA

The analysis of the COS G130M data of NGC 3783 presented in Fox et al. (2018) yields a slightly lower S II column density than our analysis of the STIS E140M data (COS: $\log N(\text{S II}) = 14.41 \pm 0.12$; STIS: $\log N(\text{S II}) = 14.57 \pm 0.03$), although both studies use the same S II line at 1253.8 Å. In Fig. B1 we compare the STIS E140M data with the COS G130M data in the spectral region around the S II λ 1253.8 line to explore the origin for this discrepancy. As can be seen, the COS data are slightly more noisy than the STIS data. There also are some continuum undulations present and less absorption is seen in the line centers in the COS data, particularly in the region of the LA II absorption near 1254.8 Å. The observed discrepancies between both data sets can be explained by the lower spectral resolution of the COS data ($R \approx 15,000$ for COS vs. $R \approx 45,000$ for STIS) in combination with COS fixed-pattern features that are present in many COS data sets (e.g., Richter et al. 2017).